

TARGET DETECTION IN MULTISTATIC RADAR NETWORKS

A THESIS SUBMITTED TO  
THE GRADUATE SCHOOL OF NATURAL AND APPLIED SCIENCES  
OF  
MIDDLE EAST TECHNICAL UNIVERSITY

BY

ANIL ARSLAN

IN PARTIAL FULFILLMENT OF THE REQUIREMENTS  
FOR  
THE DEGREE OF MASTER OF SCIENCE  
IN  
ELECTRICAL AND ELECTRONICS ENGINEERING

AUGUST 2025



Approval of the thesis:

**TARGET DETECTION IN MULTISTATIC RADAR NETWORKS**

submitted by **ANIL ARSLAN** in partial fulfillment of the requirements for the degree of **Master of Science in Electrical and Electronics Engineering Department, Middle East Technical University** by,

Prof. Dr. N. Emre Altun  
Dean, Graduate School of **Natural and Applied Sciences** \_\_\_\_\_

Prof. Dr. N. Güneri Gençer  
Head of Department, **Electrical and Electronics Engineering** \_\_\_\_\_

Prof. Dr. A. Özgür Yılmaz  
Supervisor, **Electrical & Electronics Engineering, METU** \_\_\_\_\_

**Examining Committee Members:**

Prof. Dr. Berkan Dülek  
Electrical & Electronics Engineering, Hacettepe University \_\_\_\_\_

Prof. Dr. A. Özgür Yılmaz  
Electrical & Electronics Engineering, METU \_\_\_\_\_

Assist. Prof. Dr. G. Muzaffer Güvensen  
Electrical & Electronics Engineering, METU \_\_\_\_\_

Date:29.08.2025

**I hereby declare that all information in this document has been obtained and presented in accordance with academic rules and ethical conduct. I also declare that, as required by these rules and conduct, I have fully cited and referenced all material and results that are not original to this work.**

Name, Surname: Anıl Arslan

Signature :

## **ABSTRACT**

### **TARGET DETECTION IN MULTISTATIC RADAR NETWORKS**

Arslan, Anıl

M.S., Department of Electrical and Electronics Engineering

Supervisor: Prof. Dr. A. Özgür Yılmaz

August 2025, 74 pages

Advances in military technology have made possible targets with reduced back scattering coefficient, which is increasingly challenging for conventional radar systems. Although previously developed and deployed, multistatic radar networks can overcome these challenges and have gained renewed interest thanks to advances in hardware and signal processing. These networks offer superior detection performance for low-radar-cross-section targets compared to conventional monostatic radar systems, thanks to their spatially distributed nodes. Spatial diversity requires a wide separation between nodes relative to the target, ensuring that returns are independent across receivers and different sources of information about the target are available. This independence makes coherent integration for target detection impractical and eliminates the need for phase synchronization across the network, which may be challenging, especially for widely separated multistatic radar networks. As a result, techniques such as noncoherent integration and binary integration have practical importance for widely separated multistatic radar networks. On the other hand, nodes need to communicate with a fusion center for joint target detection and parameter estimation, thereby increasing the importance of optimizing communication demand. Binary integration, where only the binary result of target presence at each receiver is sent to

the fusion center, is the most communication-efficient approach, but with very coarse of information. In contrast, noncoherent integration utilizes more information and requires more communication load. This thesis examines performance metrics both theoretically and through simulation, for widely separated multistatic networks under different integration techniques and different node configurations.

**Keywords:** Multistatic radar, Distributed target detection, Selective square law integration, Spatial diversity, Phase Synchronization

## ÖZ

### MULTİSTATİK RADAR AĞLARINDA HEDEF TESPİTİ

Arslan, Anıl

Yüksek Lisans, Elektrik ve Elektronik Mühendisliği Bölümü

Tez Yöneticisi: Prof. Dr. A. Özgür Yılmaz

Ağustos 2025 , 74 sayfa

Askerî teknolojideki gelişmeler, saçılma katsayısı azaltılmış hedeflerin mümkün hâle gelmesini sağlamış ve bu durum, geleneksel radar sistemleri için giderek daha büyük bir zorluk oluşturmaya başlamıştır. Daha önce geliştirilip sahaya sürülmüş olmasına rağmen, multistatik radar ağları bu zorlukların üstesinden gelebilmekte ve donanım ile işaret işleme alanındaki ilerlemeler sayesinde yeniden ilgi görmektedir. Bu ağlar, alıcı ve vericilerden oluşan uzamsal olarak dağılmış düğümleri sayesinde, düşük radar kesit alanına sahip hedeflerin tespitinde geleneksel monostatik radar sistemlerine kıyasla daha üstün bir performans sunar. Uzamsal çeşitlilik, hedefe göre düğümler arasında büyük mesafe gerektirir; bu sayede alıcılardaki yansımalar birbirinden bağımsız olur ve hedef hakkında farklı bilgi kaynakları elde edilir. Bu bağımsızlık, hedef tespiti için faz uyumlu entegrasyonu pratik olmaktan çıkarır ve ağ genelinde faz senkronizasyonu ihtiyacını ortadan kaldırır bu, özellikle geniş alanlara yayılmış multistatik radar ağları için, zorlayıcı olabilir. Bu nedenle, faz senkronizasyonu gerektirmeyen faz uyumsuz entegrasyon ve ikili entegrasyon gibi teknikler, geniş alanlara yayılmış multistatik radar ağları için pratik önem taşımaktadır. Öte yandan, düğümlerin hedef tespiti ve parametre kestirimi için bir füzyon merkezine bilgi aktarması gereklidir;

bu da iletiřim yknn optimize edilmesini nemli hle getirir. Her bir alıcıdan yalnızca hedefin varlığına iliřkin ikili bir sonucun gnderildiđi ikili entegrasyon, iletiřim aısından en verimli yaklařımdır; ancak ok kaba bilgiye sahiptir. Buna karřılık, faz uyumsuz entegrasyon daha fazla bilgi kullanır ve daha yksek bir iletiřim yk gerektirir. Bu tez, farklı entegrasyon teknikleri ve dđm konfigrasyonları altında, geniř alanlara yayılmıř multistatik ađların performans ltlerini hem teorik olarak hem de benzetim yoluyla incelemektedir.

Anahtar Kelimeler: Multistatik radar, Dađıtık hedef tespiti, Seici karesel tmleřtirme, Uzamsal eřitlilik, Faz Eřzamanlaması

To my family

## ACKNOWLEDGMENTS

First and foremost, I would like to express my gratitude to my supervisor Prof. Dr. A. Özgür Yılmaz for his support and guidance at every stage of my graduate studies. His creative suggestions and encouragement kept me on the right track.

I would like to thank you my colleagues from ASELSAN, especially to Berkcan Özen, Engin Esen, İbrahim Bıyıklı, Mehmet Zeki Ürgüp, Tarık Keleş and Mehmet Yasin Özkan. They have always supported and motivated me whenever I needed them.

Last but not least, I am deeply grateful to my beloved family. My parents Saliha and Rüştü, my brother Ferhat and my sister Sena, and my cousin Mertcan Demir supported and motivated me unconditionally through my education.

## TABLE OF CONTENTS

ABSTRACT . . . . .	v
ÖZ . . . . .	vii
ACKNOWLEDGMENTS . . . . .	x
TABLE OF CONTENTS . . . . .	xi
LIST OF TABLES . . . . .	xiv
LIST OF FIGURES . . . . .	xv
LIST OF ABBREVIATIONS . . . . .	xix
CHAPTERS	
1 INTRODUCTION . . . . .	1
1.1 Motivation and Problem Definition . . . . .	1
1.2 Contributions and Novelties . . . . .	2
1.3 The Outline of the Thesis . . . . .	3
1.4 Notation . . . . .	3
2 BISTATIC RADAR FUNDAMENTALS . . . . .	5
2.1 Introduction . . . . .	5
2.2 Radar Fundamentals . . . . .	7
2.3 Signal Model . . . . .	13
2.4 Sampling of the Received Signal . . . . .	16

3	SPATIAL COHERENCE MODELING AND DETECTION ALGORITHMS	21
3.1	Introduction	21
3.2	Cell-Based Spatial Partitioning	23
3.3	Detection Framework	26
3.4	Centralized Detection Algorithms	27
3.4.1	Coherent Processing	27
3.4.2	Noncoherent Processing	29
3.5	Distributed Detection Algorithms	31
3.5.1	Binary Integration	32
3.5.2	Distributed Noncoherent Integration	36
4	PERFORMANCE ANALYSIS	37
4.1	Introduction	37
4.2	Optimal Local Detector	37
4.3	Binary Integration	38
4.3.1	Randomized Global Thresholding	39
4.3.2	Detection Performance Curves	43
4.4	Distributed Noncoherent Integration	45
4.5	Communication Performance	51
5	SIMULATION FRAMEWORK	53
6	CONCLUSIONS	63
6.1	Future Works	64
	REFERENCES	67
A	CONDITIONAL LIKELIHOOD RATIO	71

B DISTRIBUTION OF A SUM OF SHIFTED EXPONENTIAL RANDOM VARIABLES . . . . .	73
--	----

## LIST OF TABLES

### TABLES

Table 2.1	Parameters for a bistatic radar scenario to generate Fig. 2.3. . . . .	10
Table 5.1	Simulation parameters for a multistatic radar scenario. . . . .	54

## LIST OF FIGURES

### FIGURES

Figure 2.1	Bistatic radar geometry showing the transmitter at $\mathbf{p}_{\text{TX}}$ , receiver at $\mathbf{p}_{\text{RX}}$ , target at $\mathbf{p}_{\text{T}}$ , bistatic angle $\varphi$ , and the angle $\Psi$ between the target velocity vector $\mathbf{v}$ and the unit vectors, namely $\hat{\mathbf{u}}_{\text{TX}}$ , $\hat{\mathbf{u}}_{\text{RX}}$ and bistatic bisector vector $\hat{\mathbf{b}}$ . . . . .	6
Figure 2.2	Constant delay contours for a bistatic pair that has approximately 18 km separation between its nodes. . . . .	8
Figure 2.3	Constant SNR contours for a bistatic radar with parameters in Table 2.1. . . . .	10
Figure 2.4	Constant bistatic angle contours. . . . .	11
Figure 2.5	Constant Doppler shift contours for a target having a constant velocity of $\mathbf{v}_{\text{T}} = [50, -50, 0]^{\text{T}} \text{ m s}^{-1}$ and carrier frequency $f_c = 1 \text{ GHz}$ . . . . .	12
Figure 2.6	An example of bistatic resolution formed by two ellipses such that their bistatic ranges (sum of distances from focal points) are separated by an amount of range resolution which is calculated with a bandwidth $B = 1 \text{ MHz}$ . . . . .	13
Figure 2.7	An example of sampled noisy signal that contains a return of the transmitted signal after $\tau_0 = 120 \mu\text{s}$ . . . . .	17
Figure 2.8	The matched filter output for the received signal in Fig. 2.7 peaking at $k T_s = 120 \mu\text{s}$ . . . . .	18
Figure 2.9	The correlation of the known reference signal $s[n]$ with the delayed complex baseband signal $s((n - \tilde{k}) T_s)$ for $\tilde{k} \in [-0.5, 0.5]$ . . . . .	19

Figure 3.1	Cell responses with associated matched filter outputs peaking at $k T_s = 120 \mu\text{s}$ in Fig. 2.8. Power scale is in terms of dB. . . . .	25
Figure 3.2	Centralized detection flow at the Fusion Center. Raw samples are aligned and matched-filtered, whitened to form $\mathbf{g}$ , then a general weighted statistic $\Lambda = \Phi(\mathbf{f}(\mathbf{g}); \mathbf{w})$ is computed and compared to a threshold $\lambda$ for the global decision. . . . .	30
Figure 3.3	Distributed detection flow at the Fusion Center. Raw samples are aligned and matched-filtered, whitened and locally thresholded to form $\mathbf{g}$ , then a general weighted statistic $\Lambda = \Phi(\mathbf{f}(\mathbf{g}); \mathbf{w})$ is computed and compared to a threshold $\lambda_{\text{global}}$ for the global decision. . . . .	35
Figure 4.1	$P_{\text{FA}}^{\text{global}}$ vs equal $P_{\text{FA}}^{\text{local}}$ at all $M = 9$ receiving nodes for the binary combining detector that has at least desired $P_{\text{FA}}^{\text{global}} = 10^{-6}$ . Effective global threshold is calculated as $\lambda_{\text{high}}^{\text{global}} - q$ . . . . .	40
Figure 4.2	$P_{\text{D}}^{\text{global}}$ vs $P_{\text{FA}}^{\text{local}}$ of the scenario in Fig.4.1 under i.i.d. Rayleigh fluctuating with equal average SNR of $\eta = 8$ dB at all $M = 9$ receiving nodes. . . . .	41
Figure 4.3	$P_{\text{D}}^{\text{global}}$ vs $P_{\text{FA}}^{\text{local}}$ of the scenario in Fig.4.1 under i.i.d. Rayleigh fluctuating with equal average SNR of $\eta = 8$ dB at all $M = 9$ receiving nodes. . . . .	42
Figure 4.4	Probability $q$ of choosing lower threshold vs $P_{\text{FA}}^{\text{local}}$ to satisfy $P_{\text{FA}}^{\text{global}} = 10^{-6}$ for all $K 9$ rules. . . . .	42
Figure 4.5	$P_{\text{D}}^{\text{global}}$ vs $P_{\text{FA}}^{\text{local}}$ under i.i.d. Rayleigh fluctuating with equal average SNR of $\eta = 8$ dB at all $M = 9$ receiving nodes for the BC detector that has desired $P_{\text{FA}}^{\text{global}} = 10^{-6}$ using randomized thresholding. . . . .	43
Figure 4.6	$P_{\text{D}}^{\text{global}}$ vs equal $P_{\text{FA}}^{\text{local}}$ and equal average SNR of $\eta = 8$ dB under i.i.d. Rayleigh fluctuation at all receiving nodes for the binary combining detector that has $P_{\text{FA}}^{\text{global}} = 10^{-6}$ with randomized thresholding. . . . .	44

Figure 4.7	$P_D^{\text{global}}$ vs $P_{\text{FA}}^{\text{local}}$ with different average SNRs $\eta_m$ in (4.15) under independent Rayleigh fluctuation at all $M = 9$ receiving nodes for BC detector that has exactly $P_{\text{FA}}^{\text{global}} = 10^{-6}$ . . . . .	45
Figure 4.8	$P_D^{\text{global}}$ vs $P_{\text{FA}}^{\text{local}}$ with different average SNRs $\eta_m$ realized 1000 times under independent Rayleigh fluctuation at all $M = 9$ receiving nodes for BC detector that has exactly $P_{\text{FA}}^{\text{global}} = 10^{-6}$ . . . . .	46
Figure 4.9	$P_D^{\text{global}}$ vs equal average SNR $\eta$ under i.i.d. Rayleigh fluctuation at different number of receiving nodes for the square law combining detector that has $P_{\text{FA}}^{\text{global}} = 10^{-6}$ and $P_{\text{FA}}^{\text{local}} = 1$ . . . . .	47
Figure 4.10	$P_D^{\text{global}}$ vs reference average SNR $\bar{\eta}$ under independent Rayleigh fluctuation at all $M = 9$ receiving nodes for the SLC and WSLC detectors that have $P_{\text{FA}}^{\text{global}} = 10^{-6}$ and $P_{\text{FA}}^{\text{local}} = 1$ . . . . .	48
Figure 4.11	$P_D^{\text{global}}$ vs $P_{\text{FA}}^{\text{local}}$ with equal average SNR of $\eta = 10$ dB under i.i.d. Rayleigh fluctuation at all receiving nodes for the unweighted SLC (solid lines) and BC (dashed lines) detectors that have $P_{\text{FA}}^{\text{global}} = 10^{-6}$ . . . . .	49
Figure 4.12	$P_D^{\text{global}}$ vs $P_{\text{FA}}^{\text{local}}$ with different average SNRs $\eta_m$ realized 100 times under independent Rayleigh fluctuation at all $M = 9$ receiving nodes for the detectors that have exactly $P_{\text{FA}}^{\text{global}} = 10^{-6}$ . . . . .	50
Figure 4.13	$P_D^{\text{global}}$ vs $P_{\text{FA}}^{\text{local}}$ with different average SNRs $\eta_m$ realized 100 times under independent Rayleigh fluctuation at all $M = 3$ receiving nodes for the detectors that have exactly $P_{\text{FA}}^{\text{global}} = 10^{-6}$ . . . . .	50
Figure 5.1	Multistatic radar scenario with 7 receiving nodes (blue crosses) and 1 transmitting node (red cross). . . . .	53
Figure 5.2	The output of the centralized noncoherent integration applied to each CUT. Power scale is in terms of dB. . . . .	55
Figure 5.3	The output of the distributed noncoherent integration with $P_{\text{FA}}^{\text{local}} = 10^{-2}$ applied to each CUT. Power scale is in terms of dB. . . . .	55

Figure 5.4	The integer output of the binary integration with $P_{\text{FA}}^{\text{local}} = 10^{-2}$ applied to each CUT. . . . .	56
Figure 5.5	Coverage of the multistatic radar configuration for centralized noncoherent integration assuming a single target with RCS $\sigma_B = 1 \text{ m}^2$ . . . . .	57
Figure 5.6	Coverage of the multistatic radar configuration for distributed noncoherent integration assuming a single target with RCS $\sigma_B = 1 \text{ m}^2$ for $P_{\text{FA}}^{\text{local}} = 10^{-2}$ . . . . .	58
Figure 5.7	Coverage of the multistatic radar configuration for binary integration assuming a single target with RCS $\sigma_B = 1 \text{ m}^2$ for $P_{\text{FA}}^{\text{local}} = 1.4 \cdot 10^{-7}$ . . . . .	59
Figure 5.8	Coverage of the multistatic radar configuration for binary integration assuming a single target with RCS $\sigma_B = 1 \text{ m}^2$ for $P_{\text{FA}}^{\text{local}} = 1.9 \cdot 10^{-4}$ . . . . .	59
Figure 5.9	$P_{\text{D}}^{\text{global}} = 0.85$ contours for the coverage of the multistatic radar configuration assuming a single target with RCS $\sigma_B = 1 \text{ m}^2$ . . . . .	61
Figure 5.10	$P_{\text{D}}^{\text{global}} = 0.70$ contours for the coverage of the multistatic radar configuration assuming a single target with RCS $\sigma_B = 1 \text{ m}^2$ . . . . .	61

## LIST OF ABBREVIATIONS

### ABBREVIATIONS

RCS	Radar Cross Section
FC	Fusion Center
MSRS	Multisite Radar System
MIMO	Multiple Input Multiple Output
EM	Electromagnetic
SNR	Signal to Noise Ratio
RF	Radio Frequency
LFM	Linear Frequency Modulation
AWGN	Additive Gaussian White Noise
PRI	Pulse Repetition Interval
I	In-phase
Q	Quadrature
SRC	Spatial Resolution Cell
CUT	Cell Under Test
NP	Neyman-Pearson
LRT	Likelihood Ratio Test
LLR	Log Likelihood Ratio
GPS	Global Positioning System
WSLC	Weighted Square Law Combining
SLC	Square Law Combining
WBC	Weighted Binary Combining
BC	Binary Combining

EGC	Equal Gain Combining
MRC	Maximal Ratio Combining
CCDF	Complementary Cumulative Distribution Function
UMP	Uniformly Most Powerful
CA-CFAR	Cell Averaging-Constant False Alarm Rate
CPI	Coherent Processing Interval

## CHAPTER 1

### INTRODUCTION

In this chapter, the motivation behind this work is introduced. The contributions of this thesis and novelties are explained and the following chapters are outlined. In addition, the notation used in this work is given.

#### 1.1 Motivation and Problem Definition

Conventional monostatic radar systems may become disadvantageous in specific scenarios due to the co-location of transmitter and receiver. One of these drawbacks is the detection of stealth targets, which are designed to reduce their radar cross-section (RCS) towards the incident wave. Multistatic radar, with its spatially distributed architecture, offers a potential solution to this challenge. Target detection performance can be significantly improved by exploiting spatial diversity [1], [2]. The degree of achievable spatial diversity depends on the relative geometry between the target and the multistatic radar system, which favors a significant separation between transmitters and receivers. Consequently, widely distributed multistatic radars are often preferred, though they also introduce additional challenges.

A major limitation is that coherent processing of received signals is typically infeasible. Establishing precise phase synchronization across a multistatic network is technically demanding, and more critically, target returns tend to be decorrelated across receivers. As a result, the received signals are inherently noncoherent, making noncoherent detection algorithms essential. Analyzing the performance and limitations of such algorithms is therefore of primary importance.

The most basic form of noncoherent integration discards the phase information and combines only the power received across all observations. In a centralized approach, the collected data are transmitted to a fusion center (FC), which then performs detection. However, this requires a high-capacity communication link to transmit all received data to the FC. A commonly used alternative is distributed binary integration, where each receiver forwards only its local binary decision to the FC, thereby reducing communication overhead at the expense of performance.

The central challenge in multistatic radar networks is balancing detection performance with communication efficiency. In principle, the highest detection performance is obtained when each receiver forwards its entire power measurement to the FC, enabling centralized noncoherent integration. However, this requires prohibitively high communication bandwidth. At the opposite extreme, distributed binary integration allows receivers to send only their hard local decisions, minimizing communication overhead, but sacrificing detection performance.

Distributed noncoherent integration has emerged as a promising compromise. Instead of transmitting full signals or hard binary decisions, each receiver forwards its measured power levels if they decide target presence locally. Then, the FC can fuse only the sent power values so that noisy samples are effectively discarded, leading to a reduced communication rate. This approach is expected to achieve a more favorable trade-off, yet a thorough analytical comparison of these three strategies has remained limited.

This thesis addresses this gap by developing a unified analytical framework and systematically comparing centralized noncoherent integration, distributed noncoherent integration, and binary integration. By quantifying their respective detection performance and communication requirements, the work provides insight into the trade-offs that guide the design of practical multistatic radar systems.

## **1.2 Contributions and Novelties**

Our contributions are as follows:

- The tradeoff between noncoherent and binary integration schemes is studied in terms of analytical performance metrics.
- A practical application of target detection is presented in terms of multistatic radar coverage.

### 1.3 The Outline of the Thesis

In Chapter 2, the fundamentals of bistatic radars, the building blocks of multistatic radars, are explained. The radar range equation, propagation characteristics, and Doppler frequency shifts are calculated and compared with the monostatic radar. Then, a narrowband signal model is defined, and a vector representation of the observed data is developed.

In Chapter 3, detection schemes and different detection algorithms are discussed. The region of interest is divided into cells that form a grid, and the detection problem is formulated for each probed cell. Optimal detection algorithms for centralized and distributed detection are derived using an independent spatially incoherent signal model.

In Chapter 4, the performance of the detection algorithms in terms of target detection probability is discussed. Binary integration with randomized thresholding is introduced. Finally, the performance of detection algorithms is compared, including in terms of communication rate requirement.

In Chapter 5, an application to the multistatic radar scenario is simulated, coverage maps for detection algorithms are generated, and the results are discussed.

In Chapter 6, a summary of the studies is presented, the results are concluded, and possible future studies are mentioned.

### 1.4 Notation

Bold lowercase letters like  $\mathbf{y}$  denote column vectors and bold uppercase letters like  $\mathbf{Y}$  denote matrices. The transpose, conjugate, and Hermitian transpose operators for

matrices and vectors are denoted by  $(\cdot)^\top$ ,  $(\cdot)^*$ , and  $(\cdot)^\dagger$ , respectively. In addition,  $j$  is used as the imaginary unit.

## CHAPTER 2

### BISTATIC RADAR FUNDAMENTALS

#### 2.1 Introduction

A radar is fundamentally composed of a transmitter that generates an electromagnetic wave propagating through space and a receiver that collects the reflected waves to infer information about the environment, and then presents results to the radar operator. Processing of the received data depends on the desired radar task, the most elementary one being the finding of the position of targets. A radar can also perform a variety of more complex tasks, ranging from terrain mapping and weather prediction to military target tracking or identification.

Multistatic radar systems are presented in [3] and their applications in [4] and [5]. These works establish the fundamental foundation of multistatic radar theory. The classification of radar systems is important in establishing standard definitions to avoid ambiguity. [3, Chapter 1.1] makes this classification and collects all possible configurations of multistatic radar systems under the term multisite radar system (MSRS).

Firstly, if the radar system has a single transmitter and a single receiver located at the same position, then these systems are called monostatic radars. A monostatic radar can also utilize more than one antenna, so it can operate as a phased array or collocated multiple-input-multiple-output (MIMO) radar [6]. Monostatic radars are well studied and the most common class of radar systems. Secondly, this single transmitter and single receiver can be located at different positions, resulting in a bistatic radar. Thanks to geometric separation, a bistatic radar may benefit from advantages that will be discussed in this chapter. The term node will be used to indicate radar components

at distinct locations, so there are three types of nodes, namely the transmitting node, the receiving node, and the monostatic node. A monostatic node is a special case when the distance between a receiving node and a transmitting node approaches zero.

A collection of different nodes constitutes an MSRS, but a key feature should be emphasized. Suppose that all receiving nodes can process the returns caused by all the transmitting nodes in the system, including transmitters and receivers of a monostatic node. In that case, such a system is a multistatic radar. As a counterexample, it is also possible that multiple monostatic nodes operate independently but work cooperatively and exchange information as a networked system, but this is not classified as a multistatic radar.

The theory of bistatic radars is essential for understanding multistatic radars because all transmitter-receiver pairings in the system are the fundamental building blocks of a multistatic radar. In this chapter, a signal model based on the geometry and physics of propagation will be developed for a single bistatic pair. The physical laws of wave propagation determine the capabilities of the radar and directly influence optimal signal processing techniques. Therefore, this section reviews the fundamentals of radar and constructs a mathematical signal model to derive optimal processing algorithms.

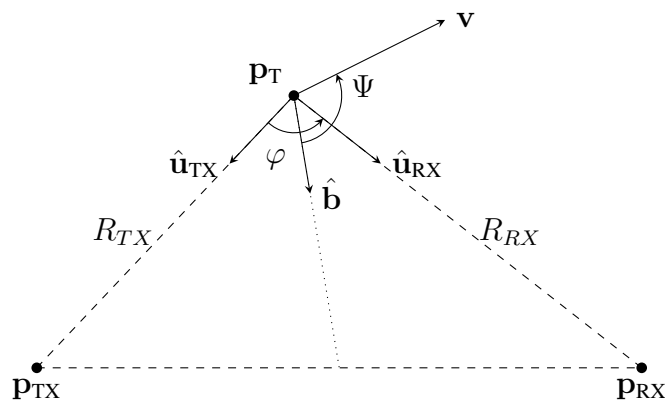


Figure 2.1: Bistatic radar geometry showing the transmitter at  $\mathbf{p}_{TX}$ , receiver at  $\mathbf{p}_{RX}$ , target at  $\mathbf{p}_T$ , bistatic angle  $\varphi$ , and the angle  $\Psi$  between the target velocity vector  $\mathbf{v}$  and the unit vectors, namely  $\hat{\mathbf{u}}_{TX}$ ,  $\hat{\mathbf{u}}_{RX}$  and bistatic bisector vector  $\hat{\mathbf{b}}$ .

## 2.2 Radar Fundamentals

As depicted in Fig. 2.1, an electromagnetic (EM) wave radiated by the transmitter at the location  $\mathbf{p}_{\text{TX}} \in \mathbb{R}^3$  will propagate with the speed of light  $c \approx 3 \cdot 10^8 \text{ m s}^{-1}$  in free space. EM waves reflect from a point target located at  $\mathbf{p}_{\text{T}} \in \mathbb{R}^3$ , and their returns will be collected by the receiver located at  $\mathbf{p}_{\text{RX}} \in \mathbb{R}^3$ . The two most fundamental quantity that a radar measures is how much time passed between the transmission and reception, as well as what portion of the transmitted power is received. The time delay can be calculated using the speed of the wave and the length of the path it travels. Therefore, the propagation delay along the transmitter-target-receiver path is given by

$$c \tau_0 = \|\mathbf{p}_{\text{T}} - \mathbf{p}_{\text{TX}}\| + \|\mathbf{p}_{\text{T}} - \mathbf{p}_{\text{RX}}\| \quad (2.1)$$

or equivalently,

$$\tau_0 = \frac{R_{\text{TX}} + R_{\text{RX}}}{c}. \quad (2.2)$$

Here, the ranges between the target and the nodes are defined as

$$R_{\text{TX}} = \|\mathbf{p}_{\text{T}} - \mathbf{p}_{\text{TX}}\|, \quad R_{\text{RX}} = \|\mathbf{p}_{\text{T}} - \mathbf{p}_{\text{RX}}\|. \quad (2.3)$$

When  $\mathbf{p}_{\text{TX}} = \mathbf{p}_{\text{RX}}$ , the range simplifies to  $R_{\text{TX}} = R_{\text{RX}} = R$ , thus the time delay for a monostatic radar is

$$\tau_0 = \frac{2R}{c}. \quad (2.4)$$

The equal time delay of a monostatic radar defines a sphere whereas that of a bistatic radar defines an ellipsoid in the space. In Fig. 2.2, the constant delay contours are presented with ellipsoids cut in the xy plane such that the transmitting and receiving nodes are at the foci of these ellipses. Throughout this chapter, the bistatic pair located as in Fig. 2.2 will be considered.

The power received will be a portion of the power transmitted  $P_{\text{TX}}$ , and the radar range equation governs this relationship. Assuming the far-field condition, the waves will spread spherically; hence, the power density (with units of  $\text{W m}^{-2}$ ) incident on a point target under free-space propagation is

$$S_{\text{TX}} = \frac{P_{\text{TX}}}{4\pi R_{\text{TX}}^2}. \quad (2.5)$$

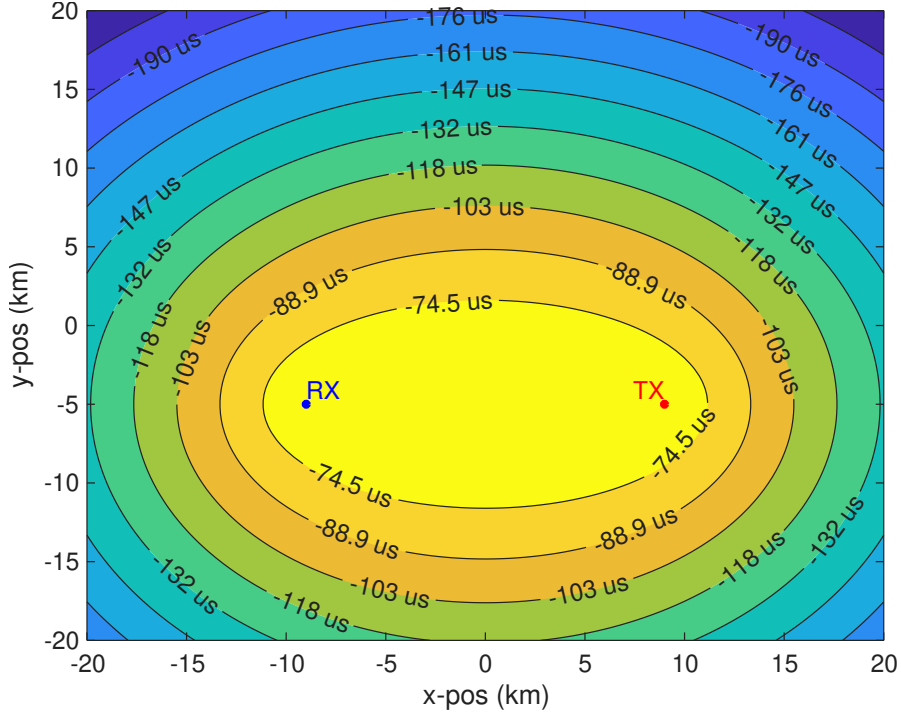


Figure 2.2: Constant delay contours for a bistatic pair that has approximately 18 km separation between its nodes.

A practical antenna will not distribute power uniformly in all directions, but it will have directionality. 2.5 should be modified with the transmitter gain  $G_{TX}$  accounting for the focussed power at the target location. The target then receives and reradiates the incoming power proportional to its effective area, known as the RCS (radar cross section)  $\sigma_B$ . Finally, the power reflected from the target also spreads spherically; thus, the power density at the receiver becomes

$$S_{RX} = \frac{S_{TX}\sigma_B}{4\pi R_{RX}^2} = \frac{P_{TX}G_{TX}\sigma_B}{(4\pi)^2 R_{TX}^2 R_{RX}^2}. \quad (2.6)$$

The effective aperture  $A_e$  of a receiver with gain  $G_{RX}$  is

$$A_e = \frac{G_{RX}\lambda_c^2}{4\pi} \quad (2.7)$$

where  $\lambda_c = c/f_c$  is the carrier wavelength. Thus, the received power is

$$P_{RX} = S_{RX}A_e = \frac{P_{TX}G_{TX}G_{RX}\lambda_c^2\sigma_B}{(4\pi)^3 R_{TX}^2 R_{RX}^2}, \quad (2.8)$$

which defines the bistatic radar range equation. For a monostatic radar the radar equation becomes the following,

$$P_{RX}^{mono} = \frac{P_{TX}G_{TX}G_{RX}\lambda_c^2\sigma_M}{(4\pi)^3 R^4} \quad (2.9)$$

where  $\sigma_M$  is the monostatic RCS, a special case of  $\sigma_B$ . The ratio of received power and internal noise power  $P_N$  is the signal-to-noise ratio (SNR) and quantifies the detectability in the radar. In practice, the noise power can be calculated as

$$P_N = k T_0 B_{RX} \quad (2.10)$$

where  $k \approx 1.38 \cdot 10^{-23} \text{ J K}^{-1}$  is Boltzmann constant. The equivalent noise temperature  $T_0$  can be taken as 290 K for practical purposes.  $B_{RX}$  is the bandwidth of the receiver [7, Chapter 2.4].

From equation (2.8) the SNR becomes

$$\text{SNR} = \frac{P_{RX}}{P_N} = \frac{P_{TX} G_{TX} G_{RX} \lambda_c^2 \sigma_B}{(4\pi)^3 R_{TX}^2 R_{RX}^2 k T_0 B_{RX}}. \quad (2.11)$$

The surfaces defined by equal SNR points create spheres for the monostatic radar, similar to the constant delay surfaces. However, these surfaces become complex for a bistatic radar, which means that they do not have the same form as the constant delay surfaces. Hence, separation between transmitter and receiver causes a huge change in the properties of the radar. For a bistatic radar, Fig. 2.3 shows the constant SNR contours called Cassini ovals. Table 2.1 contains used radar parameters to generate constant SNR contours.

The bistatic angle  $\varphi$  in Fig. 2.1 affects the value of  $\sigma_B$ . It is the central geometric quantity in bistatic radar systems because it also affects other aspects of radar performance, including resolution and Doppler shift characteristics. It is defined as the angle formed at the target between the transmitter and receiver lines of sight such that

$$\cos \varphi = \hat{\mathbf{u}}_{TX}^\top \hat{\mathbf{u}}_{RX}, \quad \varphi \in [0, \pi] \quad (2.12)$$

where

$$\hat{\mathbf{u}}_{TX} = \frac{\mathbf{p}_{TX} - \mathbf{p}_T}{\|\mathbf{p}_{TX} - \mathbf{p}_T\|}, \quad \hat{\mathbf{u}}_{RX} = \frac{\mathbf{p}_{RX} - \mathbf{p}_T}{\|\mathbf{p}_{RX} - \mathbf{p}_T\|}. \quad (2.13)$$

For monostatic radars,  $\varphi$  always equals  $0^\circ$ , therefore,  $\sigma_B$  always equals  $\sigma_M$ . However, bistatic radars have the ability to receive power with different  $\varphi$  leading to different  $\sigma_B$  which may be advantageous compared to monostatic radars. Under certain conditions, there is a relationship between  $\sigma_B$  and  $\sigma_m$  measurements [8] which is applied in [9] and [10]. There are three main cases of bistatic angle. The first is back scattering geometry or monostatic-like geometry for  $\varphi \approx 0^\circ$ . The receiving node seems

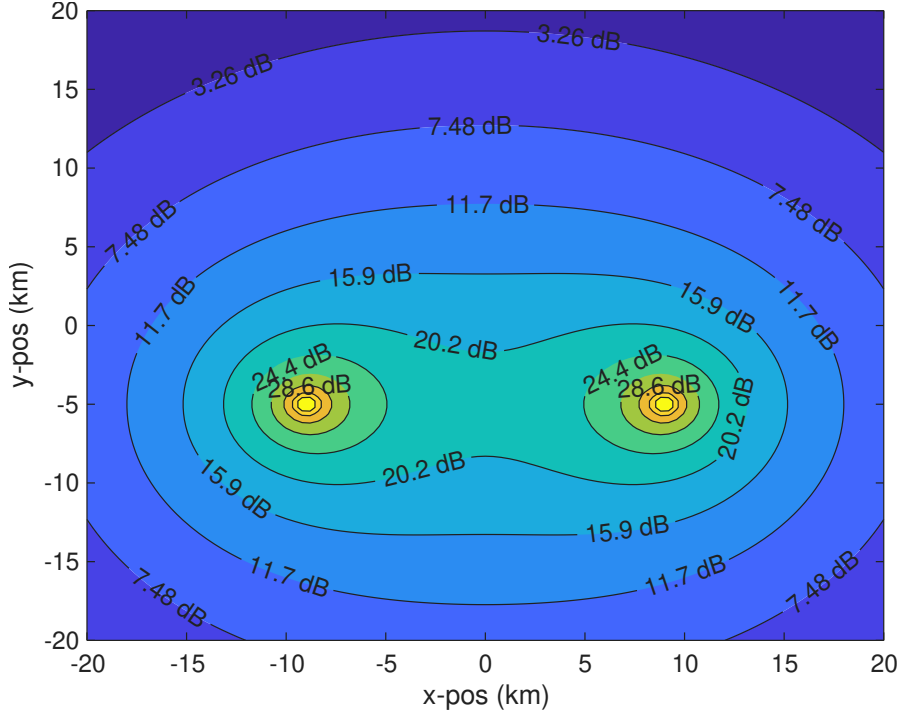


Figure 2.3: Constant SNR contours for a bistatic radar with parameters in Table 2.1.

closer to the transmitting node from the perspective of the target even if the separation between nodes is high and the observed RCS becomes approximately the monostatic RCS. Secondly, when  $\varphi \approx 180^\circ$ , geometry becomes forward scattering. The receiving node and the transmitting node are on opposite sides of the target. Often resulting in strong returns due to the large RCS [11]. Finally,  $\varphi = 90^\circ$  is a side scattering geometry that offers a different resolution and Doppler characteristics. Similarly to Figures 2.2 and 2.3, the constant bistatic angle contours are shown in 2.4.

Table 2.1: Parameters for a bistatic radar scenario to generate Fig. 2.3.

Parameter	Symbol	Value
Transmitted power	$P_{TX}$	40 kW
Antenna gains	$G_{TX}, G_{RX}$	$\approx 13$ dBi
Carrier frequency	$f_c$	1 GHz
Bandwidth of the receiver	$B_{RX}$	1 MHz
Radar cross section	$\sigma_B$	5 m <sup>2</sup>

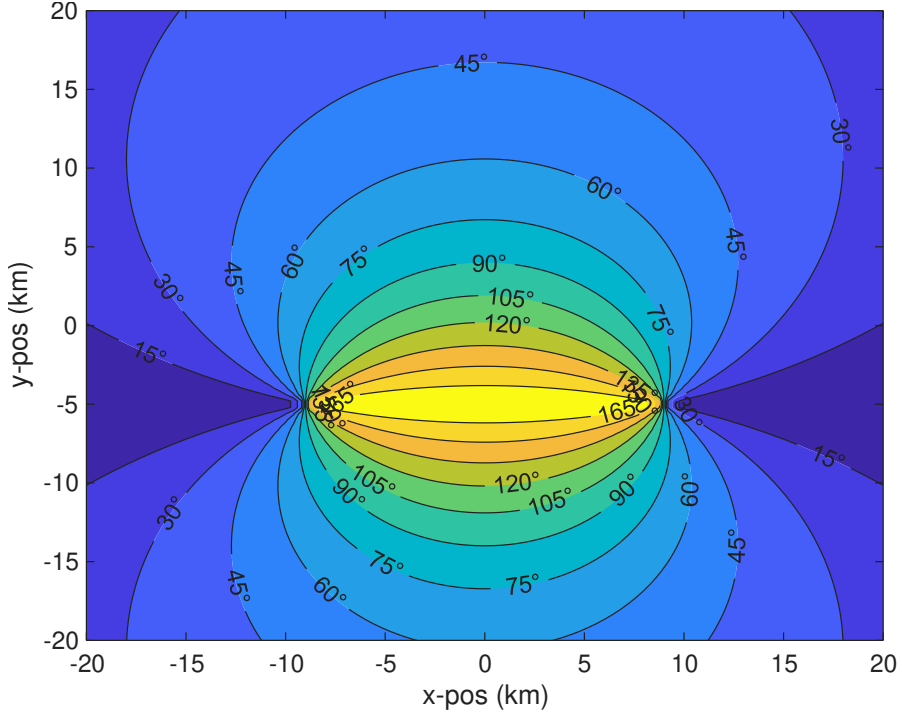


Figure 2.4: Constant bistatic angle contours.

Due to target motion, Doppler frequency shift emerges on the received signal. The amount of shift will be proportional to the radial velocity of the target along  $\hat{\mathbf{u}}_{\text{TX}}$  and  $\hat{\mathbf{u}}_{\text{RX}}$  in (2.13). Thus, the magnitude of Doppler is shaped by  $\varphi$ . The resulting Doppler frequency due to the target velocity  $\mathbf{v}_{\text{T}} \in \mathbb{R}^3$  is

$$f_d = -\frac{1}{\lambda_c} (\hat{\mathbf{u}}_{\text{TX}} + \hat{\mathbf{u}}_{\text{RX}})^{\top} \mathbf{v}_{\text{T}}. \quad (2.14)$$

To interpret this geometrically, let us define the bistatic Doppler bisector as

$$\hat{\mathbf{b}} = \frac{\hat{\mathbf{u}}_{\text{TX}} + \hat{\mathbf{u}}_{\text{RX}}}{\|\hat{\mathbf{u}}_{\text{TX}} + \hat{\mathbf{u}}_{\text{RX}}\|}. \quad (2.15)$$

Let us call the angle between the velocity vector  $\mathbf{v}_{\text{T}}$  and the bisector vector  $\hat{\mathbf{b}}$  as  $\Psi$  as in Fig. 2.1, then the Doppler frequency shift becomes

$$f_d = \frac{2}{\lambda_c} \|\mathbf{v}_{\text{T}}\| \cos \frac{\varphi}{2} \cos \Psi. \quad (2.16)$$

The Doppler shift is maximized when the target velocity is aligned with  $\hat{\mathbf{b}}$  and vanishes when it is orthogonal. Also, when the target is in the forward scattering region, the Doppler shift disappears. In the monostatic-like region, the formula (2.16) reduces

the monostatic Doppler shift given by

$$f_d = \frac{2}{\lambda_c} \|\mathbf{v}_T\| \cos \Psi = \frac{2}{\lambda_c} \mathbf{v}_T^\top \hat{\mathbf{r}}_{TX} = \frac{2}{\lambda_c} \mathbf{v}_T^\top \hat{\mathbf{r}}_{RX}. \quad (2.17)$$

For a specific target velocity  $\mathbf{v}_T$ , an example of constant Doppler shift curves in the  $xy$  plane is shown in Fig. 2.5.

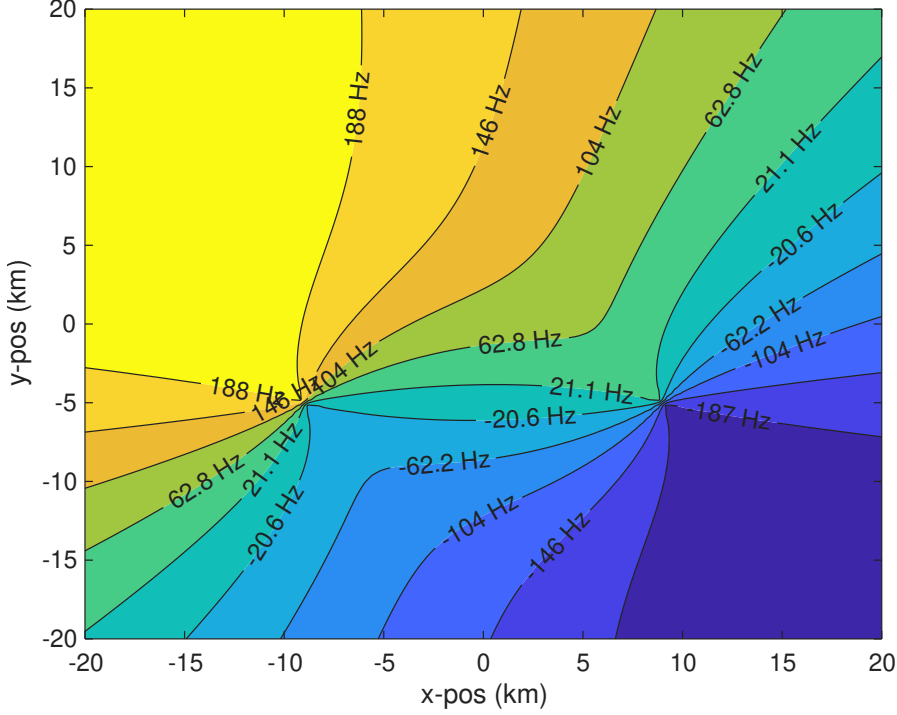


Figure 2.5: Constant Doppler shift contours for a target having a constant velocity of  $\mathbf{v}_T = [50, -50, 0]^\top \text{ m s}^{-1}$  and carrier frequency  $f_c = 1 \text{ GHz}$ .

Range resolution quantifies the degree of target separation capability of the radar, and is determined by the bandwidth  $B$  of the transmitted signal. For a bistatic radar, the range resolution also depends on the bistatic angle  $\varphi$ . From the geometry of the constant delay surfaces in Fig. 2.2, the effective resolution along the bistatic range axis can be written as

$$\Delta R = \frac{c}{2B \cos(\varphi/2)}. \quad (2.18)$$

For  $\varphi = 0^\circ$ , the range resolution becomes the well-known monostatic range resolution of  $\Delta R = c/(2B)$ . As  $\varphi$  increases, the range resolution degrades. In the forward scattering region, the range resolution becomes unbounded. In Fig. 2.6, the resolution of the bistatic range is illustrated using two constant delay ellipses such that both have

the same focal points, but the difference between the sum of distances from the focal points is equal to the range resolution in (2.18).

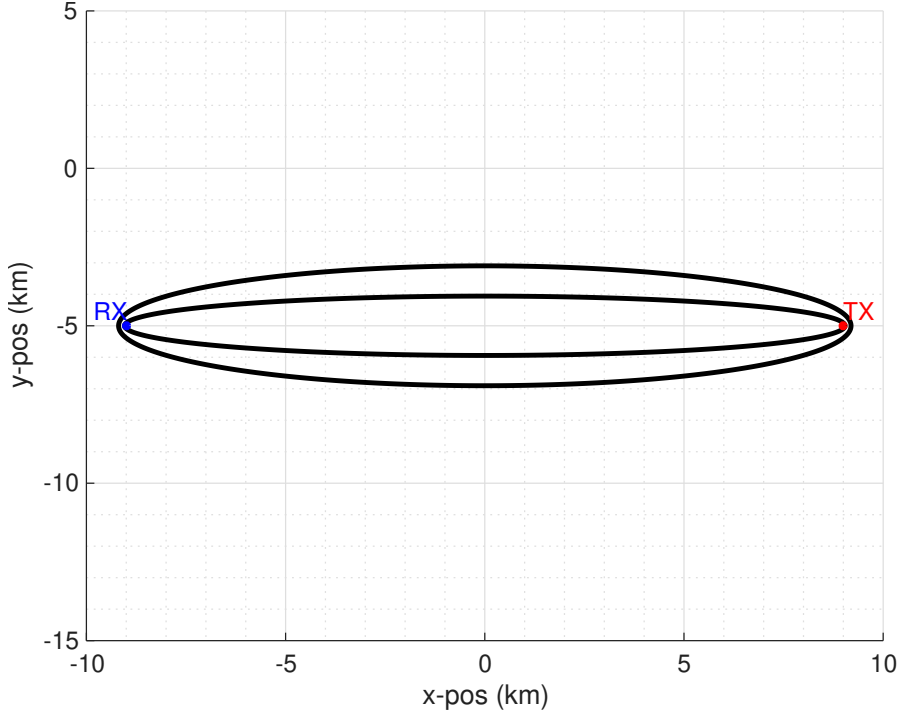


Figure 2.6: An example of bistatic resolution formed by two ellipses such that their bistatic ranges (sum of distances from focal points) are separated by an amount of range resolution which is calculated with a bandwidth  $B = 1$  MHz .

### 2.3 Signal Model

Radars may emit electromagnetic waves continuously or send pulses periodically. The pulse generation procedure starts with the generation of a coded baseband signal with duration  $T_{PW}$ . After mixing with the carrier frequency, the real-valued passband signal is called a radio frequency (RF) signal, and it is transmitted by the radar system using antennas. Then, the single RF pulse with starting time  $t_{TX}$  of transmission can be expressed as

$$u(t) = \text{Re} \left\{ s(t - t_{TX}) e^{j2\pi f_c(t - t_{TX})} \right\}, \quad t_{TX} \leq t \leq t_{TX} + T_{PW} \quad (2.19)$$

where  $s(t)$  denotes a complex baseband signal (that is, the low pass equivalent) with unit energy, and  $f_c$  is the carrier frequency in Hz. The total transmitted energy  $E_{\text{total}}$

of  $s(t)$  can be calculated as

$$E_{\text{total}} = \int_{t_{\text{TX}}}^{t_{\text{TX}}+T_{\text{PW}}} |s(t)|^2 dt = 1. \quad (2.20)$$

The instantaneous power  $|s(t)|^2$  of a constant envelope signal must be  $1/T_{\text{PW}}$  to satisfy the unit energy condition.

This baseband representation enables simplified mathematical modeling of modulation and propagation effects while retaining all physically relevant information about the transmitted signal. There are many coding schemes for  $s(t)$ , such as the linear frequency modulated (LFM) pulse waveform, which is one of the most common. Specifically, symmetric LFM of duration  $T_{\text{PW}}$  and bandwidth  $B$  is utilized which can be written as

$$s(t) = \frac{1}{\sqrt{T_{\text{PW}}}} \exp\left(j\pi \frac{B}{T_{\text{PW}}} (t - T_{\text{PW}}/2)^2\right), \quad 0 \leq t \leq T_{\text{PW}}. \quad (2.21)$$

The envelope of  $s(t)$  is chosen as constant without loss of generality. The instantaneous frequency  $f_{\text{inst}}(t)$  can be calculated by taking the derivative of the instantaneous phase  $\phi_{\text{inst}}(t)$  as

$$f_{\text{inst}}(t) = \frac{1}{2\pi} \frac{d\phi_{\text{inst}}(t)}{dt} = \frac{B}{T_{\text{PW}}} (t - T_{\text{PW}}/2), \quad 0 \leq t \leq T_{\text{PW}}, \quad (2.22)$$

The frequency sweep is symmetric around  $t = T_{\text{PW}}/2$ , and it is linear from  $-B/2$  to  $B/2$ .

Throughout this work, the radar is assumed to operate under the narrowband assumption, defined by the inequality  $B \ll f_c$ . This assumption implies that all spectral components of  $s(t)$  experience approximately the same phase delay, allowing compact and tractable signal models [6, Chapter 4.2]. Hence, the received low-pass equivalent single pulse from a single scatterer can be modeled as

$$x(t) = A s(t - t_{\text{TX}} - \tau_0) e^{-j2\pi f_c \tau_0}, \quad t_{\text{RX}} \leq t \leq t_{\text{RX}} + T_{\text{RX}} \quad (2.23)$$

where  $A \in \mathbb{C}$  is the complex gain depending on the radar range equation which also includes the phase change induced by the scatterer. The receiver starts receiving at  $t_{\text{RX}}$  and listens for a duration  $T_{\text{RX}}$ . The exponential term accounts for the carrier phase shift induced by the constant propagation delay. When the target is in motion, the propagation delay  $\tau_0$  changes with time, introducing a Doppler shift as in (2.14). If

the total change  $\tau_0$  is much shorter than the inverse of the bandwidth  $B$ , the effect of the Doppler shift on  $s(t - t_{\text{TX}} - \tau_0)$  is negligible. However, if  $\tau_0$  changes in a way comparable to the wavelength, then it induces a phase modulation in the received signal [7, Chapter 2.6.1]. Thus, the Doppler-modulated received signal can be expressed as

$$x(t) = A s(t - t_{\text{TX}} - \tau_0) e^{-j2\pi f_c \tau_0} e^{j2\pi f_d (t - t_{\text{TX}} - \tau_0)}, \quad t_{\text{RX}} \leq t \leq t_{\text{RX}} + T_{\text{RX}}. \quad (2.24)$$

Introducing receiver internal thermal noise as additive white Gaussian noise (AWGN) final form of the received signal without processing becomes

$$x(t) = A s(t - t_{\text{TX}} - \tau_0) e^{-j2\pi f_c \tau_0} e^{j2\pi f_d (t - t_{\text{TX}} - \tau_0)} + w(t), \quad t_{\text{RX}} \leq t \leq t_{\text{RX}} + T_{\text{RX}}. \quad (2.25)$$

(2.25) is the general expression for the received signal model to a single transmitted pulse. In practice, more than one pulse is repeated periodically with a period called the pulse repetition interval (PRI). In addition, the Doppler effect becomes dominant between pulses and can be neglected during the short duration of the pulse width  $T_{\text{PW}}$  (stop-and-hop assumption in [7, Chapter 2.6.2]). Hence, for a total of  $N_p$  pulses, the phase induced by the Doppler effect can be written as

$$2\pi f_d t = 2\pi f_d n_p \quad n_p = 0, 1, \dots, N_p - 1 \quad (2.26)$$

where  $n_p$  is the pulse index. When multiple pulses are used, the Fourier transform can be applied to find the Doppler frequency shift  $f_d$ . In addition, there is a coherent processing gain of  $N_p$ , since the Fourier transform collects the input SNR per pulse into a higher output SNR in the frequency bin corresponding to  $f_d$ .

In the following chapters, the detection performance analysis curves are generated using output SNR values where prior processing is not important. This thesis also does not investigate the estimation of the target velocity; hence, analysis for a single pulse will be enough, and results of the thesis can be easily extended for multiple pulses. Therefore, (2.25) can be simplified as follows

$$x(t) = A s(t - t_{\text{TX}} - \tau_0) e^{-j2\pi f_c \tau_0} e^{-j2\pi f_d (t_{\text{TX}} + \tau_0)} + w(t), \quad t_{\text{RX}} \leq t \leq t_{\text{RX}} + T_{\text{RX}}. \quad (2.27)$$

Let us collect all terms without time dependence into the complex gain coefficient  $h$  so that (2.27) becomes

$$x(t) = h s(t - t_{\text{TX}} - \tau_0) + w(t) \quad t_{\text{RX}} \leq t \leq t_{\text{RX}} + T_{\text{RX}}. \quad (2.28)$$

The squared magnitude of  $h$  is the received power calculated from equation (2.8). The phase of  $h$  depends on the phase changes due to the velocity and position of the target as well as the phase induced during scattering.

## 2.4 Sampling of the Received Signal

To facilitate digital signal processing, the received signal  $x(t)$  is sampled at a rate  $f_s = 1/T_s$ , then discrete time samples  $x[n] = x(nT_s + t_{\text{RX}})$  of the received signal become

$$x[n] = h s(nT_s + t_{\text{RX}} - t_{\text{TX}} - \tau_0) + w(nT_s + t_{\text{RX}}), \quad n = 0, 1, \dots, N - 1. \quad (2.29)$$

Here,  $n$  is the sample index and  $N$  is the total number of temporal samples in a given listening duration  $T_{\text{RX}} = NT_s$ . The term  $t_{\text{RX}} - t_{\text{TX}}$  can be used to model time synchronization and should be chosen according to the desired region of interest. In this thesis, receiving begins at the end of the transmission so that  $t_{\text{RX}} = 0$  and  $t_{\text{TX}} = -T_{\text{PW}}$ .

Throughout the thesis, cooperative signal reception will be analyzed; hence the temporal structure of the deterministic waveform is known. Let us define  $s[n]$  as the sampled version of the known complex baseband signal  $s(t)$  at the time instants  $t = 0, T_s, \dots, T_{\text{PW}} - T_s$ . Therefore,  $s[n] = s(nT_s)$  for  $n = 0, 1, \dots, N_{\text{PW}} - 1$ , and the pulse width in terms of the number of samples is  $N_{\text{PW}} = T_{\text{PW}}/T_s$ .

If all samples of the known reference signal  $s[n]$  have the same magnitude (constant envelope), then the energy per sample  $|s[n]|^2 = 1/N_{\text{PW}}$  because  $T_s |s(nT_s)|^2 = T_s/T_{\text{PW}} = 1/N_{\text{PW}}$ . Therefore, the unit energy condition of (2.20) can be expressed for  $s[n]$  as follows

$$\sum_{n=0}^{N_{\text{PW}}-1} |s[n]|^2 = 1. \quad (2.30)$$

Assuming integer sample shift  $n_0 = \tau_0 f_s \in \mathbb{Z}$  and i.i.d. noise samples  $w[n] = w(nT_s + t_{\text{RX}}) \sim \mathcal{CN}(0, \sigma^2)$  with a circularly symmetric complex Gaussian distribution, the received signal using  $t_{\text{RX}} = 0$  and  $t_{\text{TX}} = -T_{\text{PW}}$  can be written as

$$x[n] = h s[n - n_0 + N_{\text{PW}} - 1] + w[n], \quad n = 0, 1, \dots, N - 1. \quad (2.31)$$

The input SNR per sample right after sampling and before any processing is defined as

$$\text{SNR}_{in} = \frac{\mathbb{E}[|h s[n - n_0 + N_{\text{PW}} - 1]|^2]}{\mathbb{E}[|w[n]|^2]} = \frac{|h|^2}{N_{\text{PW}}\sigma^2}, \quad (2.32)$$

for  $n = n_0 - N_{\text{PW}} + 1, \dots, n_0 - 1, n_0$ . In the case of sampling with the Nyquist rate  $f_s = B_{\text{RX}} = B$ ,  $\text{SNR}_{in}$  can be calculated directly from (2.11).

Fig. 2.7 illustrates an example of a received signal normalized to the noise power and sampled at a rate  $f_s = 1$  MHz such that  $N_{\text{PW}} = 10$  and  $N = 250$ . The received waveform is delayed with  $\tau_0 = 120 \mu\text{s}$  so that  $n_0 = 120$ . The radar parameters in Table 2.1 are used to generate the received signal.

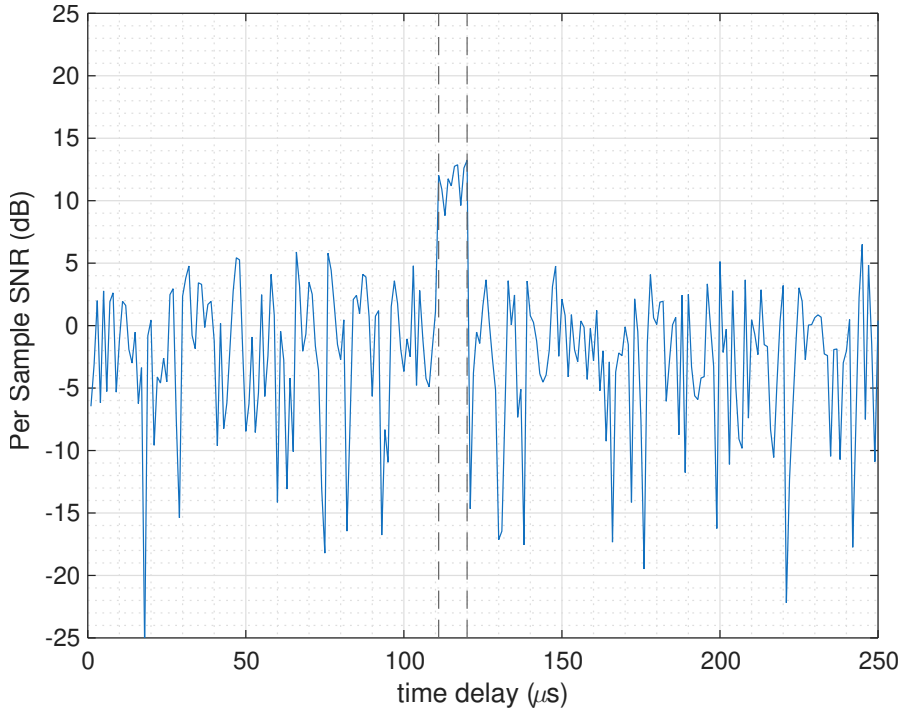


Figure 2.7: An example of sampled noisy signal that contains a return of the transmitted signal after  $\tau_0 = 120 \mu\text{s}$ .

The bistatic radar can exploit the information of known waveform structure through a matched filtering operation as follows,

$$y[k] = \sum_{n=0}^{N_{\text{PW}}-1} s^*[n] x[n + k - N_{\text{PW}} + 1] \quad k = 0, 1, \dots, N - 1. \quad (2.33)$$

This operation is optimal filtering that maximizes the output SNR under i.i.d.  $w[n] \sim \mathcal{CN}(0, \sigma^2)$ . Substituting the received signal (2.31), the output of the matched filter

becomes

$$y[k] = h \sum_{n=0}^{N_{\text{PW}}-1} s^*[n] s[n+k-n_0] + \tilde{w}[k] \quad (2.34)$$

where the second term, noise after matched filtering, is

$$\tilde{w}[k] = \sum_{n=0}^{N_{\text{PW}}-1} s^*[n] w[n+k-N_{\text{PW}}+1]. \quad (2.35)$$

The first term is the discrete autocorrelation of the known reference signal,

$$r[k-n_0] = \sum_{n=0}^{N_{\text{PW}}-1} s^*[n] s[k+n-n_0], \quad r[0] = 1, \quad (2.36)$$

which attains its maximum at  $k = n_0$ . For unit total energy  $s[n]$  as in (2.30),  $r[0] = 1$  is the maximum possible value of the autocorrelation result. Then, at  $k = n_0$ , the output of the matched filter is

$$y[n_0] = h + \sum_{n=0}^{N-1} s^*[n] w[n+n_0] = h + \tilde{w}[n_0]. \quad (2.37)$$

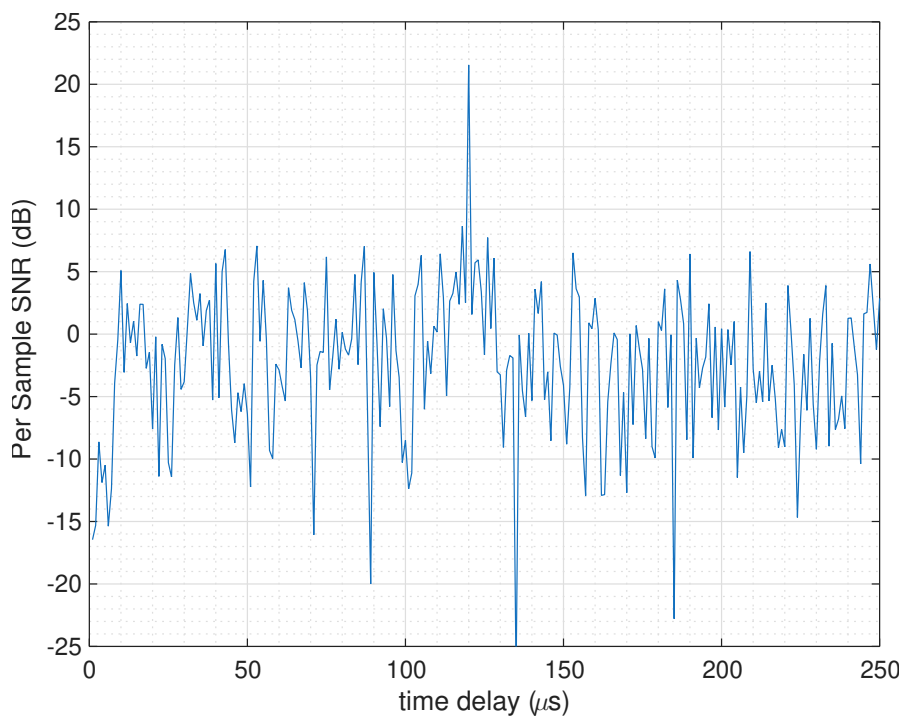


Figure 2.8: The matched filter output for the received signal in Fig. 2.7 peaking at  $k T_s = 120 \mu\text{s}$ .

The output SNR per sample after matched filtering can be calculated as

$$\text{SNR}_{\text{output}} = \frac{\mathbb{E}[|h|^2]}{\mathbb{E}[|\tilde{w}[n_0]|^2]} = \frac{|h|^2}{\sigma^2}, \quad k = n_0. \quad (2.38)$$

When comparing (2.32) and (2.38), the SNR per sample is improved by a factor of  $N_{\text{PW}}$ . Fig. 2.8 shows the output of the matched filter of the received signal in Fig. 2.7. When comparing the figures, the matched filtering integrates all the distributed energy distributed  $N_{\text{PW}}$  samples of  $x[n]$  into a single sample corresponding to the time delay of  $\tau_0$ . Hence, the location of the peak of the matched filter output can be used to estimate the bistatic range of the target using (2.1).

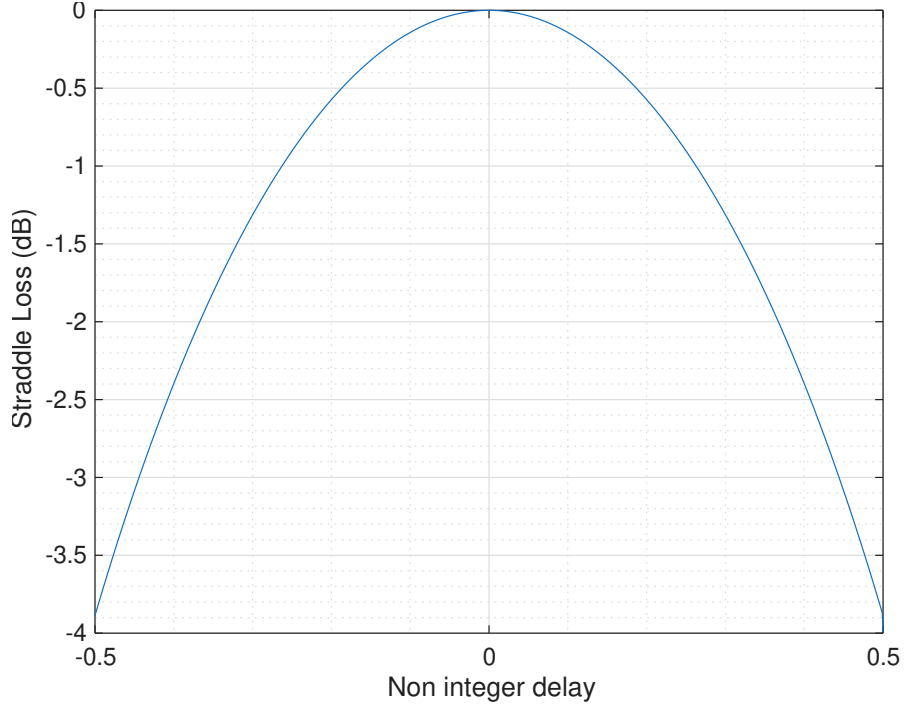


Figure 2.9: The correlation of the known reference signal  $s[n]$  with the delayed complex baseband signal  $s((n - \tilde{k}) T_s)$  for  $\tilde{k} \in [-0.5, 0.5]$ .

If  $\tau_0 f_s$  is not an integer, then the matched filtering cannot perfectly overlap with the received signal. In this case, the output SNR is degraded by an amount called straddle loss, which can be calculated as

$$r(\tilde{k}) = \sum_{n=0}^{N_{\text{PW}}-1} s^*[n] s((\tilde{k} - n) T_s), \quad (2.39)$$

where the non-integer sample shift  $\tilde{k}$  is  $\tau_0 f_s - \text{round}(\tau_0 f_s) \in [-0.5, 0.5]$  and the function  $\text{round}(\cdot)$  finds the nearest integer. Fig. 2.9 shows the autocorrelation of (2.21)

with  $\tilde{k}$  between  $-0.5$  and  $0.5$ . The maximum straddle loss is approximately 4dB, therefore, the improvement in SNR can be between  $10 \log N_{\text{PW}} = 10\text{dB}$  without straddle loss and 6dB with the maximum straddle loss.

Finally, samples of the output of the matched filter can be collected in a temporal observation vector as

$$\mathbf{y} = [y[0], \dots, y[N-1]]^\top \in \mathbb{C}^{N \times 1}. \quad (2.40)$$

Similarly, autocorrelation and noise vectors can be defined as follows

$$\mathbf{r} = [r[0], \dots, r[N-1]]^\top \in \mathbb{C}^{N \times 1}, \quad (2.41)$$

$$\tilde{\mathbf{w}} = [\tilde{w}[0], \dots, \tilde{w}[N-1]]^\top \in \mathbb{C}^{N \times 1}. \quad (2.42)$$

Then, the observation vector for a bistatic pair can be written compactly as

$$\mathbf{y} = h \mathbf{r} + \tilde{\mathbf{w}}. \quad (2.43)$$

## CHAPTER 3

### SPATIAL COHERENCE MODELING AND DETECTION ALGORITHMS

#### 3.1 Introduction

This chapter focuses on statistical detection techniques applied to the signal model (2.43) developed in Chapter 2. The architecture of the detection algorithms plays a critical role in shaping the performance, bandwidth requirements, and implementation complexity of multistatic radar systems. A central unit called the fusion center (FC) collects information from all receiving nodes and interprets the environment. The form of available data in the FC determines the fusion level and dictates the type of detector that can be implemented. Three primary levels of data processing are commonly encountered in multistatic radar systems [12].

- **Coherent Integration:** Complex samples of the temporal observation vector  $\mathbf{y}_m \in \mathbb{C}^N$  from each receiving node are transmitted to the FC without any local processing. Since each sample contains both in-phase (I) and quadrature (Q) components, this approach offers the highest information content, thus providing the optimal detection performance. However, this fusion algorithm requires high-rate data links, precise timing alignment, and carrier phase synchronization among all nodes. More importantly, the signal itself should be coherent; therefore, bistatic RCS at each receiver should not be decorrelated.
- **Noncoherent Integration:** In this setting, the receiving nodes locally compute a detection statistic (for example, signal energy) and transmit it to the FC. These statistics are often real-valued, nonnegative envelopes of the observed signal with discarded phase information. In spatially noncoherent radar networks where phase differences between receivers are unknown or random, these statis-

tics that exclude the phase may carry all the usable information about the target; hence, this fusion level can provide statistically optimal detection performance. In addition, the communication burden is reduced compared to coherent integration.

- **Binary Integration:** In this fusion technique, each receiver applies a local threshold and generates a binary decision. Only these binary outcomes are transmitted to the FC, where logical decision rules such as "or", "and", or majority voting are applied. This type of fusion imposes minimal requirements on communication and synchronization but may suffer from limited detection performance due to the severe information loss associated with binary quantization.

Although coherent integration is ideal for phase-synchronized coherent networks, noncoherent integration provides a highly efficient alternative when phase alignment is impractical. Binary integration is suitable for low-resource or large-scale networks where minimal communication overhead is critical.

Centralized detection refers to systems where complete observed data from spatially distributed receivers are transmitted to the FC, but no local detection occurs. FC performs joint signal processing to make a global decision. Such signal processing algorithms require high communication load and computational resources. Centralized detection enables statistically optimal rules, assuming the availability of the necessary synchronization and communication infrastructure. However, distributed detection delegates partial or complete detection tasks to individual receivers. Each node processes its locally received signal to generate test statistics data, which is forwarded to the FC. In the end, the final decision on the presence of the target is still made in the FC. [13]

Coherent and noncoherent integration are centralized detection algorithms, but binary integration is a distributed detection algorithm because each receiver performs a local detection and sends only binary results. Other local information such as fusion weights can be sent together with the local detection results to be used in FC. Then FC makes a global detection by combining the received binary results. If the received power values are sent for only local detections, then noncoherent integration can be performed at FC which will be called distributed noncoherent integration which has

reduced communication load compared to centralized noncoherent integration. The performance of distributed noncoherent integration is shown to be between binary integration and centralized noncoherent integration.

### 3.2 Cell-Based Spatial Partitioning

In order to perform detection over a parameter space, the region of interest can be divided into a finite set of spatial resolution cells (SRCs) discussed in [14], each of which is probed independently. The set of all cells considered can be denoted as

$$\mathcal{C} = \{c_1, c_2, \dots, c_J\} \quad (3.1)$$

where each  $c_j \in \mathbb{R}^Q$  corresponds to a specific tuple formed by  $Q$  different parameters. For example, these parameters can be velocity or position in Cartesian coordinates. For the purpose of this thesis, the set of cells will be formed by two-dimensional position vectors on the  $xy$  plane.

In multistatic radar configurations, multiple spatially separated receivers observe reflections from a common transmitter-target interaction. These observations differ in propagation delay, Doppler shift, and complex gain. Let us denote the number of receivers with  $M$  and their indices as  $m$ , then define the spatial gain matrix as

$$\mathbf{H} = \text{diag}(h_1, \dots, h_M) \in \mathbb{C}^{N \times M}. \quad (3.2)$$

Samples of  $\mathbf{H}$  may be subject to randomness due to propagation uncertainties or imperfect receiver synchronization.

For a given cell under test (CUT)  $c_j$ , the expected time delay  $\tau_m^{(j)}$  for each receiver will be determined by the geometry of the multistatic configuration. Denote the temporal sample closest to  $\tau_m^{(j)}$  as  $k_m^{(j)}$ . The FC then processes the related part of the temporal observation vectors (2.43) by pulling the corresponding samples for each receiver. Specifically, the spatial observation vector corresponding to the probed  $j$ th cell can be written as

$$\mathbf{y}^{(j)} = [y_1[k_1^{(j)}], \dots, y_M[k_M^{(j)}]]^\top \in \mathbb{C}^{M \times 1} \quad (3.3)$$

Then a detection rule is applied to  $\mathbf{y}^{(j)}$  for each SRC to decide whether a target is present. If the processing technique requires known deterministic parameters, such

as time delays, phase shifts, and power levels, these quantities can be computed on the basis of the geometry of the hypothesized target location (i.e., the center of the SRC).

Let us define vectors

$$\mathbf{r}^{(j)} = [r_1[k_1^{(j)}], \dots, r_M[k_M^{(j)}]]^\top \in \mathbb{C}^{M \times 1}, \quad (3.4)$$

$$\mathbf{w}^{(j)} = [w_1[k_1^{(j)}], \dots, w_M[k_M^{(j)}]]^\top \in \mathbb{C}^{M \times 1}, \quad (3.5)$$

so that the spatial observation vector can be expressed as

$$\mathbf{y}^{(j)} = \mathbf{H} \mathbf{r}^{(j)} + \mathbf{w}^{(j)}. \quad (3.6)$$

Let us assume that the spatial noise vector  $\mathbf{w}^{(j)} \in \mathbb{C}^{M \times 1}$  has the same diagonal stationary noise covariance matrix  $\Sigma \in \mathbb{C}^{M \times M}$  for all cells,

$$\Sigma = \text{diag}(\sigma_1^2, \dots, \sigma_M^2), \quad \sigma_m^2 \in \mathbb{R}_+. \quad (3.7)$$

The set  $\mathbb{R}_+$  denotes positive real numbers. Since the statistical behavior of  $\mathbf{w}^{(j)}$  does not change from cell to cell,  $(j)$  will be removed in the rest of the thesis and simply  $\mathbf{w} \sim \mathcal{CN}(0, \Sigma)$  will be used.

Assume a target is exactly at the center of a probed cell and time delays are multiples of the sampling period as  $\tau_m^{(j)} f_s = k_m^{(j)}$ . Then all entries in the vector  $\mathbf{r}^{(j)}$  turn out to be 1 from (2.36) and the spatial observation vector simplifies to

$$\mathbf{y}^{(j)} = \mathbf{h} + \mathbf{w}, \quad \mathbf{h} = [h_1, \dots, h_M]^\top. \quad (3.8)$$

This is the optimal scenario where any SNR degradation does not occur, and optimal detectors will be designed for this case. On the other hand, if  $\tau_m^{(j)} f_s$  is not an integer, the SNR improvement factor becomes less than  $N_{\text{PW}}$  with an amount called straddle loss which is discussed in (2.39). Whenever  $r[k]$  in (2.36) is evaluated other than 0, performance loss will occur due to degraded SNR and this is the case because it is very unlikely that all receivers sample the received signal without any straddle loss.

In addition, all receivers must be time-aligned to a common sampling grid, in other words, time synchronization must be established. This ensures that the temporal samples that form the probed spatial observation vector  $\mathbf{y}^{(j)}$  in (3.3) are aligned across

the receivers. Nowadays, time synchronization can be easily established and [15] provides a related work.

Using the mapped spatial observation vector for each SRC, a target response map can be generated as

$$\mathbf{Z} = [\mathbf{y}^{(1)}, \dots, \mathbf{y}^{(J)}] \in \mathbb{C}^{M \times J} \quad (3.9)$$

Fig. 3.1 illustrates the image of  $|\mathbf{Z}|$  constructed using the positions indicated by each SRC for the example bistatic radar from the previous chapter. The cell grid is uniformly divided with a spacing of 150m, which is equal to the minimum range resolution of the bistatic radar as in (2.18). [16] proposes a methodology to determine an efficient grid structure such that cell crossing losses are controlled, but a uniform grid will work fine for the purpose of this thesis. In addition, the targets will be modeled exactly at the center of the cells because this requires a separate analysis for off-grid cases.

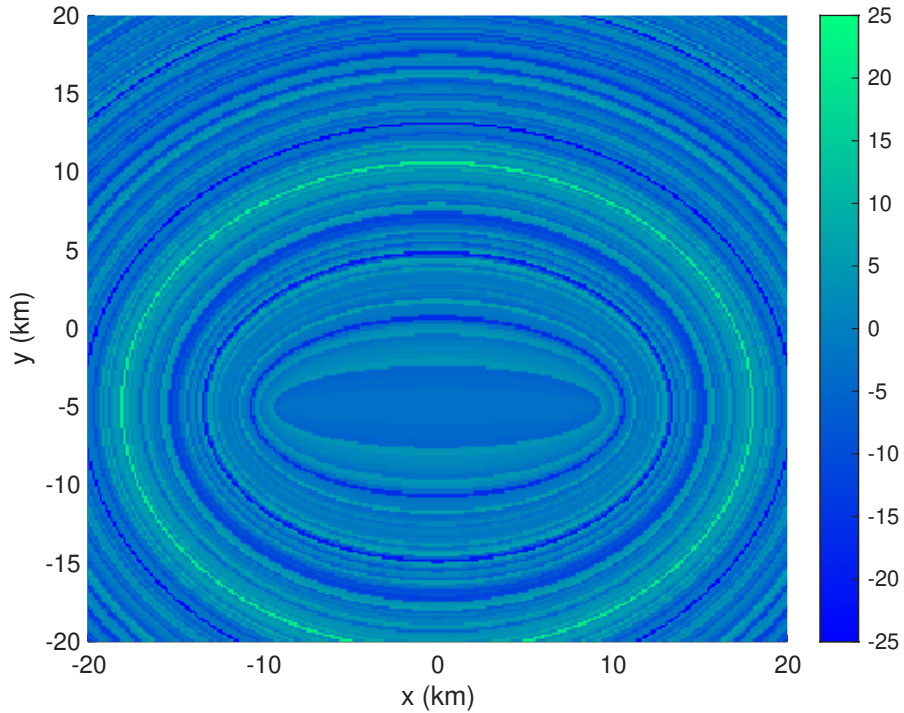


Figure 3.1: Cell responses with associated matched filter outputs peaking at  $k T_s = 120 \mu\text{s}$  in Fig. 2.8. Power scale is in terms of dB.

### 3.3 Detection Framework

In radar target detection, the objective is to decide between two competing hypotheses based on the observation vector for a CUT. Two hypotheses can be formed for  $\mathbf{y}^{(j)} \in \mathbb{C}^{M \times 1}$  in (3.8) as

$$\mathcal{H}_0 : \text{Target absent} \quad \Rightarrow \quad \mathbf{y}^{(j)} = \mathbf{w}, \quad (3.10)$$

$$\mathcal{H}_1 : \text{Target present} \quad \Rightarrow \quad \mathbf{y}^{(j)} = \mathbf{h} + \mathbf{w}. \quad (3.11)$$

The Neyman-Pearson (NP) criterion seeks to maximize the probability of detection  $P_D$  subject to a fixed constraint on the probability of false alarm  $P_{FA} \leq P_{FA}^{desired}$ , where  $P_{FA}^{desired} \in (0, 1)$  is a design parameter. According to the NP lemma, the optimal decision rule is the likelihood ratio test (LRT) [17, Chapter 2.2],

$$\Lambda(\mathbf{y}^{(j)}) = \frac{f(\mathbf{y}^{(j)} | \mathcal{H}_1)}{f(\mathbf{y}^{(j)} | \mathcal{H}_0)} \underset{\mathcal{H}_0}{\overset{\mathcal{H}_1}{\gtrless}} \lambda \quad (3.12)$$

where  $f(\mathbf{y}^{(j)} | \mathcal{H}_i)$  denotes the likelihood under hypothesis  $\mathcal{H}_i$ , and  $\lambda$  is a threshold chosen to satisfy the false alarm constraint. This form is optimal with complete knowledge of the statistical distributions.

From (A.5) in Appendix A, the conditional log-likelihood ratio (LLR) can be written as

$$\ln \Lambda(\mathbf{y}^{(j)} | \mathbf{h}) = 2\Re \{ \mathbf{h}^\dagger \Sigma^{-1} \mathbf{y}^{(j)} \} - \mathbf{h}^\dagger \Sigma^{-1} \mathbf{h}. \quad (3.13)$$

To analyze phase and magnitude across receivers separately, let us define the diagonal spatial phase matrix,

$$\mathbf{U} = \text{diag}(\mathbf{u}) = \text{diag}(e^{j\phi_1}, \dots, e^{j\phi_M}), \quad \phi_m \in [0, 2\pi), \quad (3.14)$$

and, spatial gain vector as,

$$\boldsymbol{\alpha} = [\alpha_1, \dots, \alpha_M]^\top, \quad \alpha_m \in \mathbb{R}_+. \quad (3.15)$$

Then the complex spatial gain vector represented in polar form becomes

$$\mathbf{h} = \boldsymbol{\alpha}^\top \mathbf{U}, \quad \text{with } h_m = \alpha_m e^{j\phi_m}. \quad (3.16)$$

Instead of working with raw signal power, it is more intuitive and elegant to work with SNR. Let us collect the output SNR per node in (2.38) in a vector as

$$\boldsymbol{\rho} = [\rho_1, \dots, \rho_M]^\top, \quad \rho_m = \frac{\alpha_m^2}{\sigma_m^2} \in \mathbb{R}_+, \quad (3.17)$$

and, create the vector consisting of square root of the SNR values,

$$\boldsymbol{\gamma} = [\gamma_1, \dots, \gamma_M]^\top, \quad \gamma_m = \frac{\alpha_m}{\sigma_m} \in \mathbb{R}_+, \quad \text{so that } \rho_m = \gamma_m^2. \quad (3.18)$$

Let us define the whitened spatial complex gain vector as

$$\tilde{\mathbf{h}} = \boldsymbol{\gamma}^\top \mathbf{U}, \quad \text{with } \tilde{h}_m = \gamma_m e^{j\phi_m}. \quad (3.19)$$

Finally, define the whitened matched filter output vector using the standard deviation of noise as follows

$$\mathbf{g} = [g_1, \dots, g_M]^\top \in \mathbb{C}^{M \times 1}, \quad \text{with } g_m = \frac{\mathbf{y}_m^{(j)}}{\sigma_m}. \quad (3.20)$$

Then, the conditional LLR in (3.13) becomes

$$\ln \Lambda(\mathbf{y}^{(j)} | \boldsymbol{\gamma}, \mathbf{U}) = 2 \Re \{ \boldsymbol{\gamma}^\top \mathbf{U}^\dagger \mathbf{g} \} - \boldsymbol{\gamma}^\top \boldsymbol{\gamma}. \quad (3.21)$$

Scalars such as the term  $\boldsymbol{\gamma}^\top \boldsymbol{\gamma}$  do not change the detection performance, so they can be dropped because a modified threshold  $\lambda$  can be utilized. Therefore, the final form of the optimal detector becomes

$$\Lambda_{known} = \Re \{ \boldsymbol{\gamma}^\top \mathbf{U}^\dagger \mathbf{g} \}. \quad (3.22)$$

This expression emphasizes the influence of phase shifts (via  $\mathbf{U}$ ) and square root SNR scaling (via  $\boldsymbol{\gamma}$ ) on the whitened matched filter output  $\mathbf{g}$ , forming a spatially whitened, coherently aligned test statistics. Finally, the marginalized likelihood ratio can be expressed in terms of marginalization in the square root SNR vector  $\boldsymbol{\gamma}$  and the spatial phase matrix  $\mathbf{U} = \text{diag}(\mathbf{u})$ . Assuming statistical independence between  $\boldsymbol{\gamma}$  and  $\mathbf{U}$ , the resulting unconditional likelihood ratio becomes

$$\Lambda(\mathbf{y}^{(j)}) = \int \int \exp [2 \boldsymbol{\gamma}^\top \Re \{ \mathbf{U}^\dagger \mathbf{g} \}] p_{\mathbf{u}}(\mathbf{u}) p_{\boldsymbol{\gamma}}(\boldsymbol{\gamma}) d\mathbf{u} d\boldsymbol{\gamma}. \quad (3.23)$$

This form explicitly separates the contributions of phase uncertainty and SNR variation to the detection problem.

## 3.4 Centralized Detection Algorithms

### 3.4.1 Coherent Processing

For a fully known complex spatial gain vector  $\mathbf{h}$ , the optimal test statistic follows directly from the conditional LLR in equation (3.22). This case provides the most

favorable setting for coherent signal processing. It allows the radar network to exploit all magnitude and phase information between receivers for optimal detection. Although a fully known complex spatial gain vector model may not be practical in most real-world applications, it provides a valuable benchmark that serves with upper performance limits.

In practice, the complex spatial gain vector  $\mathbf{h}$  is known in all receivers up to a common complex gain  $\beta$ . This condition arises in tightly synchronized radar networks where the reflected signal structure is preserved across the nodes and can be modeled as a single complex-valued gain multiplying a known spatial signature vector. To analyze the effect of this common complex scalar, let us modify the whitened complex spatial gain model in equation (3.19) as

$$\tilde{\mathbf{h}} = \beta \bar{\mathbf{h}} = \beta \bar{\boldsymbol{\gamma}}^T \bar{\mathbf{U}}, \quad (3.24)$$

where the spatial phase matrix in equation (3.14) is modified as follows,

$$\mathbf{U} = e^{j\theta} \bar{\mathbf{U}} = e^{j\theta} \text{diag}(1, e^{j\bar{\phi}_2}, \dots, e^{j\bar{\phi}_M}), \quad \theta, \bar{\phi}_m \in [0, 2\pi) \quad (3.25)$$

with the known phases  $\bar{\phi}_m$  relative to a reference receiver (here, first receiver) and the common phase  $\theta$ . Similarly, the square root SNR vector in (3.18) is modified as follows,

$$\boldsymbol{\gamma} = |\beta| \bar{\boldsymbol{\gamma}}, \quad \|\bar{\boldsymbol{\gamma}}\| = 1, \quad (3.26)$$

where  $|\beta|$  is the common spatial gain and  $\bar{\boldsymbol{\gamma}}$  is the normalized square root SNR vector consisting of known relative spatial gains.

Except for the fully known  $\beta$ , all coherent processing detectors in any model of  $\beta$  practically turn out to be [3, Chapter 5.2]

$$\Lambda_{coh} = \left| \bar{\boldsymbol{\gamma}}^T \bar{\mathbf{U}}^\dagger \mathbf{g} \right|. \quad (3.27)$$

(3.8) generalizes the signal model of a phased array that receives a plane wave from a known direction. In that case,  $\bar{\mathbf{U}}$  corresponds to a steering vector, and coherent summation over its entries enables beamforming gain. Hence, the structure of (3.27) resembles the beamforming operation [6]. Typical examples of radar systems obeying the coherent signal model are monostatic phased arrays via shared local oscillators, and multistatic radars using GPS-disciplined clocks or reference beacons.

Coherent processing requires a phase-synchronous multistatic radar in which all receivers are phase-aligned and referenced to a common clock or carrier. The receivers must maintain phase alignment relative to a reference oscillator or by round-trip calibration, so that the relative phases encoded in  $\bar{\mathbf{U}}$  are not degraded by independent receiver drifts. In addition, all receivers must share a common carrier frequency or have calibrated offsets. This allows the relative phases to be fixed and known across the multistatic radar.

In addition, the received signal must remain spatially coherent between the receivers. This typically necessitates that the receivers be closely spaced relative to the target to ensure that the signal remains correlated by preventing spatial decorrelation caused by different aspect angles. Therefore, for widely separated multistatic radar systems spatially coherent models fail since each receiver observes the target from a different angle most of the time. Even if spatial decorrelation was not occurring, it would be challenging to establish phase synchronization for such widely separated receivers as well. This motivates other signal models, which relax or eliminate the assumptions of spatial coherence.

### 3.4.2 Noncoherent Processing

In multistatic radar systems, noncoherent signal modeling is required if spatial phase coherence is absent due to system-level asynchrony or spatial incoherence of the signal return. Depending on the behavior of the SNR variation across receivers, two cases are possible. The first case models partially correlated SNR values for closely spaced nodes where each bistatic pair evaluates similar bistatic RCS  $\sigma_B$  of the target. In the second case, spatial observations consist of fully decorrelated complex gains across receivers arising in widely separated multistatic radar networks. Detection strategies accommodate randomness in the spatial gain vector  $\mathbf{h}$  usually using energy-based approaches. As phase alignment is unavailable, signal processing depends only on envelope information, such as magnitude or power, excluding spatial techniques such as beamforming. However, temporal synchronization remains crucial for maintaining coherence in temporal samples.

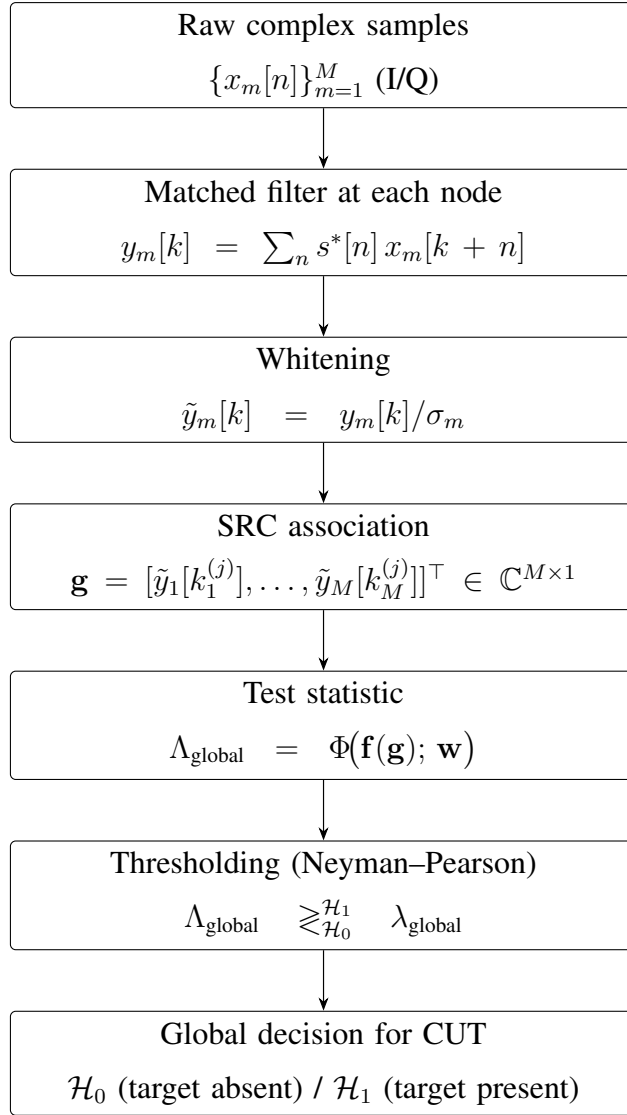


Figure 3.2: Centralized detection flow at the Fusion Center. Raw samples are aligned and matched-filtered, whitened to form  $\mathbf{g}$ , then a general weighted statistic  $\Lambda = \Phi(\mathbf{f}(\mathbf{g}); \mathbf{w})$  is computed and compared to a threshold  $\lambda$  for the global decision.

In order to model fully decorrelated spatial gain vector of widely separated multi-static radar, the most practical and mathematically elegant signal model consists of independent zero-mean circularly symmetric Gaussian entries, which is analogous to the Swerling 2 target model [7, Chapter 6.3.4], where independent probability densities are between pulses rather than between receivers. Let us assume that the complex gain vector is modeled as

$$\mathbf{h} \sim \mathcal{CN}(\mathbf{0}, \text{diag}(\eta_1, \dots, \eta_M)) \quad (3.28)$$

where  $\eta_m \triangleq \mathbb{E}[|h_m|^2]$  denotes the average SNR at the receiver  $m$ . Applying (3.12) directly using  $h_m | \mathcal{H}_0 \sim \mathcal{CN}(0, 1)$  and  $h_m | \mathcal{H}_1 \sim \mathcal{CN}(0, 1 + \eta_m)$ , the LLR turns out to be the weighted square law combiner (WSLC) as follows [3, Chapter 5.2],

$$\Lambda_{WSLC} = \sum_{m=1}^M \frac{\eta_m}{1 + \eta_m} |\tilde{g}_m|^2. \quad (3.29)$$

For an equal average SNR  $\eta_m$  at all nodes, the square law combiner (SLC) without weighting is

$$\Lambda_{SLC} = \|\mathbf{g}\|^2. \quad (3.30)$$

In practical scenarios, estimating the average SNR  $\eta_m$  for each receiver may be infeasible, since the target will change position already until enough snapshots are collected for the estimation of signal covariance. Hence a simple square law detector in equation (3.30) is the most important and practical detector for noncoherent integration.

Since the detection algorithms introduced in this section make use of all received data, they are in the class of centralized detection algorithms. Fig. 3.2 shows the general flow for centralized detection algorithms. In the next section, distributed algorithms are introduced.

### 3.5 Distributed Detection Algorithms

As developed in the previous chapter, multichannel radar data  $\mathbf{y}_m \in \mathbb{C}^{N \times 1}$  in (2.43) are associated with cells to construct  $\mathbf{Z} \in \mathbb{C}^{M \times J}$  in (3.9) at the fusion center. In centralized detection architectures, FC needs the whole  $\mathbf{y}_m$  to decide the presence of the target.

In distributed detection, full access to  $\mathbf{y}_m$  is no longer assumed. Instead, each receiver locally computes a test statistic  $\Lambda_m^{\text{local}} \in \mathbb{C}^{N \times 1}$ , applies a local threshold  $\lambda_m^{\text{local}}$ , and generates a binary indicator  $\delta_m \in \{0, 1\}^{N \times 1}$  indicating whether its measurement is considered informative. Then, the spatial observation vector  $\mathbf{y}^{(j)}$  for the probed cell in 3.3 is modified as follows

$$\mathbf{y}_{masked}^{(j)} = [y_1[k_1^{(j)}]\delta_1[k_1^{(j)}], \dots, y_M[k_M^{(j)}]\delta_M[k_M^{(j)}]]^T \in \mathbb{C}^{M \times 1}. \quad (3.31)$$

The collection of all local decisions forms the indicator vector  $\boldsymbol{\delta} = [\delta_1^{(j)}, \dots, \delta_M^{(j)}]^\top$ , with  $\delta_m^{(j)} = \delta_m[k_m^{(j)}]$  that zeros out entries of  $\mathbf{y}^{(j)}$  corresponding to the non-informative receiver. The FC then processes the masked vector  $\mathbf{y}_{masked}^{(j)}$  and makes a global detection decision. This framework captures a broad class of detection architectures, ranging from pure binary integration to centralized coherent integration, by adjusting the local thresholding policy and the global fusion function. The flow of centralized detection algorithms in Fig. 3.2 is extended for the distributed case as in Fig. 3.3.

The number of active receiving nodes for each cell  $j$  is defined as

$$K^{(j)} \triangleq \sum_{m=1}^M \delta_m^{(j)}. \quad (3.32)$$

Finally, let us also denote the set of indices of active receiving nodes as

$$\mathcal{K}^{(j)} \triangleq \{m : \delta_m^{(j)} = 1\}. \quad (3.33)$$

In the following sections, it is implicitly assumed that the  $j$ th cell is probed, and hence the superscript  $(j)$  is omitted to have neat expressions.

### 3.5.1 Binary Integration

Among distributed detection algorithms, binary integration is desirable for bandwidth or energy constrained radar networks because of its minimal communication overhead and algorithmic simplicity. However, these benefits come at the cost of reduced detection performance as a result of early quantization at the receiver level, discarding valuable information.

In the binary integration algorithm, each receiver transmits only its binary decision  $\delta_m$  to the FC instead of transmitting raw or quantized measurements. Therefore, the detection test can be formulated using LRT (3.12)

$$\Lambda^{\text{global}} = \frac{f(\boldsymbol{\delta} | \mathcal{H}_1)}{f(\boldsymbol{\delta} | \mathcal{H}_0)} \underset{\mathcal{H}_0}{\underset{\mathcal{H}_1}{\gtrless}} \lambda^{\text{global}}. \quad (3.34)$$

The local detection performance is characterized by the following probabilities,

$$P_{\text{FA},m}^{\text{local}} \triangleq \mathbb{P}(\delta_m = 1 | \mathcal{H}_0), \quad (3.35)$$

$$P_{\text{D},m}^{\text{local}} \triangleq \mathbb{P}(\delta_m = 1 | \mathcal{H}_1). \quad (3.36)$$

Let us start with the known average per node SNRs  $\eta_m$  and fixed known  $P_{FA,m}^{\text{local}}$  so that all  $P_{D,m}^{\text{local}}$  is also known. Due to spatial incoherence, binary decisions  $\delta_m$  are independent between receivers under both hypotheses. Therefore, the joint distribution of the binary vector  $\boldsymbol{\delta}$  is given by

$$f(\boldsymbol{\delta} | \mathcal{H}_i) = \prod_{m=1}^M (P_m^{(i)})^{\delta_m} (1 - P_m^{(i)})^{1-\delta_m}, \quad i \in \{0, 1\} \quad (3.37)$$

where  $P_m^{(0)} = P_{FA,m}^{\text{local}}$  and  $P_m^{(1)} = P_{D,m}^{\text{local}}$ . Substituting into (3.34), the LLR becomes

$$\Lambda^{\text{global}} = \sum_{m=1}^M \delta_m \ln \left( \frac{P_{D,m}^{\text{local}}}{P_{FA,m}^{\text{local}}} \right) + (1 - \delta_m) \ln \left( \frac{1 - P_{D,m}^{\text{local}}}{1 - P_{FA,m}^{\text{local}}} \right). \quad (3.38)$$

The LLR in (3.38) can be simplified to a weighted sum by omitting offsets, hence, weighted binary combining (WBC) becomes

$$\Lambda_{\text{WBC}} = \sum_{m=1}^M \omega_m \delta_m \quad (3.39)$$

where the fusion weights are defined as

$$\omega_m = \ln \left( \frac{P_{D,m}^{\text{local}}(1 - P_{FA,m}^{\text{local}})}{P_{FA,m}^{\text{local}}(1 - P_{D,m}^{\text{local}})} \right). \quad (3.40)$$

WBC rule is the optimal decision rule under both the Bayesian criterion (minimizing the total error probability given priors) and the Neyman-Pearson criterion (maximizing the detection probability subject to a global false alarm constraint), assuming accurate knowledge of local performance statistics [18]. Each node contributes to the decision based on its reliability.

In the special case where all local detectors exhibit identical performance, that is,  $P_{D,m}^{\text{local}} = P_D^{\text{local}}$  and  $P_{FA,m}^{\text{local}} = P_{FA}^{\text{local}}$  for all  $m$ , the weights are reduced to a constant and the fusion rule simplifies to an unweighted counting rule as

$$\Lambda_{\text{BC}} = \sum_{m=1}^M \delta_m \quad (3.41)$$

where BC stands for binary combining. This rule is known as the M out-of-N rule, where a global detection is declared if the number of local detections exceeds a fixed threshold  $\lambda^{\text{global}} \in \{0, 1, \dots, M\}$ .

For the known average per node SNRs  $\eta_m$ ,  $P_{FA,m}^{\text{local}}$  can also be optimized. Although this is outside the scope of this thesis, it was shown that joint optimization makes

use of (3.39) and the LRT of each receiver. Therefore, under equal  $\eta_m$ ,  $P_{FA,m}^{\text{local}}$  turns out to be equal  $P_{FA}^{\text{local}}$  due to symmetry [3, Chapter 6.1]. In addition, optimization in the unequal  $\eta_m$  case was shown to not produce enormous performance improvements compared to taking equal  $P_{FA}^{\text{local}}$ . Hence, from this point on, the equal  $P_{FA}^{\text{local}}$  case will be considered only.

If the target of interest changes position and orientation until enough snapshots are taken, then the estimation of  $\eta_m$  would not be practical for a radar system. Therefore,  $\Lambda_{\text{WBC}}$  will be a benchmark to compare the performance of  $\Lambda_{\text{BC}}$  under different  $\eta_m$ .

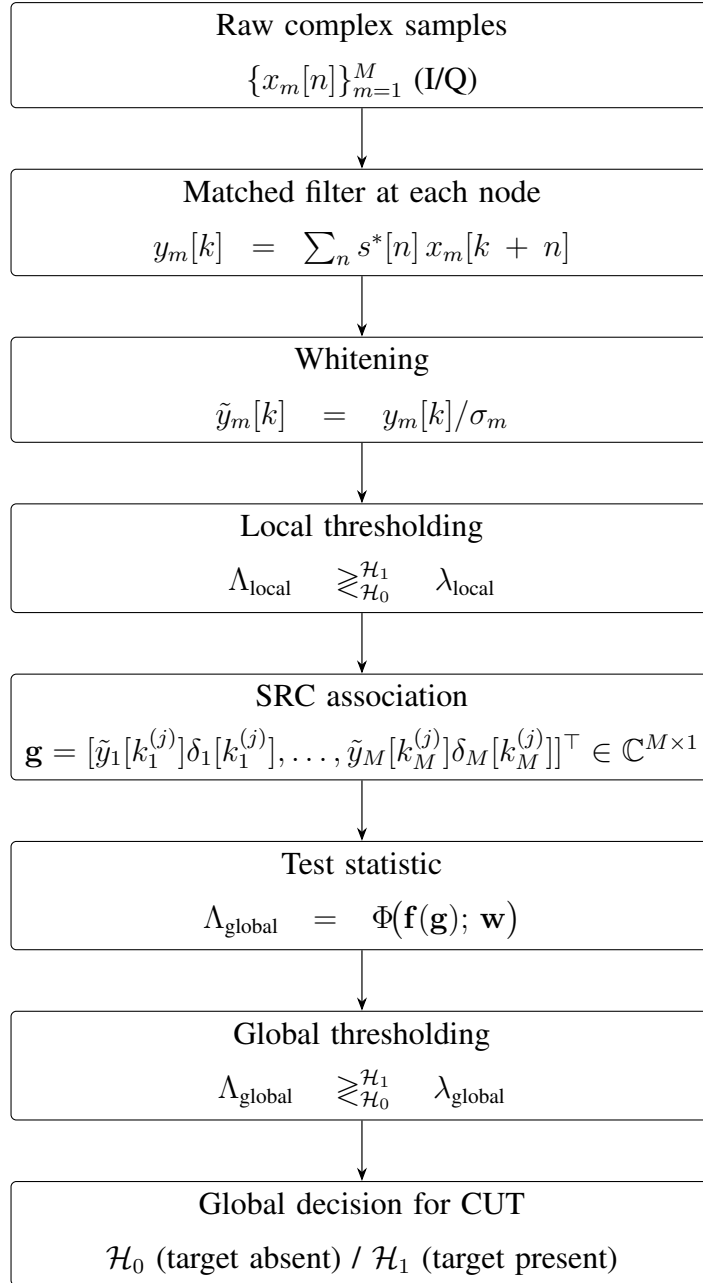


Figure 3.3: Distributed detection flow at the Fusion Center. Raw samples are aligned and matched-filtered, whitened and locally thresholded to form  $\mathbf{g}$ , then a general weighted statistic  $\Lambda = \Phi(\mathbf{f}(\mathbf{g}); \mathbf{w})$  is computed and compared to a threshold  $\lambda_{\text{global}}$  for the global decision.

### 3.5.2 Distributed Noncoherent Integration

Binary integration offers significant communication efficiency by transmitting only binary decisions. However, this approach discards the underlying analog statistics (i.e., envelope data), which may lead to deterioration in detection performance. In contrast, centralized integration techniques operate on the whole observed data  $\mathbf{y}_m$ , allowing optimal detection performance but requiring high-bandwidth communication links.

To address the trade-off between communication efficiency and detection performance, this section develops a distributed noncoherent integration architecture that specifically discards low-power statistics, typically dominated by noise, while transmitting high-power and informative statistics in analog form. This selective mechanism introduces a tunable design parameter that allows the system to trade off communication bandwidth with the global false alarm rate. The same idea is considered under cognitive radio using equal gain combining (EGC) and maximal ratio combining (MRC) techniques. [19]

Since  $\lambda_m^{\text{local}} = 0$  collapses to centralized detection, optimization of the likelihood ratio over the possible local detectors and their thresholds  $\lambda_m^{\text{local}}$  would break the assumption of distributed fusion. Hence, as the local detector LRT of  $g_m$  will be used with a fixed known nonzero  $\lambda_m^{\text{local}}$ , possibly upper bounded on bandwidth/energy constraints. The relationship between  $\lambda_m^{\text{local}}$  and communication rate is derived in Section 4.5. As a result, all centralized fusion rules will be modified by replacing the matched filter outputs  $g_m$  with masked ones  $\delta_m g_m$ . The FC observes  $g_m$  only if  $m \in \mathcal{K}$ . The condition of  $\Lambda_m^{\text{local}} > \lambda_m^{\text{local}}$  creates a truncated distribution for  $\delta_m g_m$  and determines the probability of a subset of the set  $\mathcal{K}$ .

The test statistics of the square law combining rules, namely, the SLC in (3.30) and the WSLC in (3.29) will be modified and represented by the following expression,

$$\Lambda_{\text{WSLC}} = \sum_{m \in \mathcal{K}} \omega_m |g_m|^2. \quad (3.42)$$

This test statistics modifies the centralized noncoherent integration so that summation is applied only to receivers that locally declared the presence of the target and also covers the unweighted square law combiner by choosing  $\omega_m = 1$ .

## CHAPTER 4

### PERFORMANCE ANALYSIS

#### 4.1 Introduction

This section evaluates the performance of distributed detection algorithms. The analytical expressions for the complementary cumulative distribution function (CCDF) of the test statistic are derived under both hypotheses  $\mathcal{H}_0$  and  $\mathcal{H}_1$ . These expressions facilitate the assignment of  $\lambda_m^{\text{global}}$  for a desired false alarm rate and enable the analytical characterization of the probability of detection curves  $P_D^{\text{global}}$ . Since the global test statistic  $\Lambda^{\text{global}}$  is compared to a global threshold  $\lambda^{\text{global}}$ , the resulting global performance metrics can be expressed using CCDF as

$$P_{\text{FA}}^{\text{global}}(\lambda^{\text{global}}) = \mathbb{P}(\Lambda^{\text{global}} > \lambda^{\text{global}} \mid \mathcal{H}_0) = \bar{F}_{\Lambda^{\text{global}}|\mathcal{H}_0}(\lambda^{\text{global}}), \quad (4.1)$$

$$P_{\text{D}}^{\text{global}}(\lambda^{\text{global}}) = \mathbb{P}(\Lambda^{\text{global}} > \lambda^{\text{global}} \mid \mathcal{H}_1) = \bar{F}_{\Lambda^{\text{global}}|\mathcal{H}_1}(\lambda^{\text{global}}). \quad (4.2)$$

For any distributed rule, the CCDF can be calculated by averaging the conditional CCDF of the corresponding centralized rule over all possible realizations of  $\mathcal{K}$

$$\bar{F}_{\Lambda^{\text{global}}|\mathcal{H}_i}(\lambda^{\text{global}}) = \sum_{\mathcal{K} \subseteq \{1, \dots, M\}} \bar{F}_{\Lambda^{\text{global}}|\mathcal{H}_i, \mathcal{K}}(\lambda^{\text{global}}) \mathbb{P}(\mathcal{K} \mid \mathcal{H}_i). \quad (4.3)$$

#### 4.2 Optimal Local Detector

The assumption of a known temporal structure defines  $\mathbf{y}_m$  as a matched filtered output given in (3.20), therefore, the optimal local detector depends only on the behavior of the common complex gain factor of  $\mathbf{y}_m$ . In practice, the common phase factor is unknown or random; therefore, the optimal detector reduces to a phase-invariant

magnitude test as in (3.27),

$$\Lambda_m^{\text{local}} = |g_m|^2. \quad (4.4)$$

This test is UMP (uniformly most powerful) among all phase-invariant detectors under the given model [7, Chapter 6.2.4]. For the null hypothesis  $\mathcal{H}_0$ , the test statistic (4.4) follows an exponential distribution  $|g_m|^2 \sim \text{Exp}(1)$ . The local probability of false alarm is given by

$$P_{\text{FA},m}^{\text{local}} = \exp(-\lambda_m^{\text{local}}) \quad (4.5)$$

In practice, detectors such as cell averaging constant false alarm rate (CA-CFAR) are utilized which do not require the knowledge of noise power because it calculates the noise power adaptively using measurements of neighborhood of probed time delay value. Let us now characterize the local detection probability  $P_{\text{D},m}^{\text{local}}$  and the local false alarm probability  $P_{\text{FA},m}^{\text{local}}$  relations.

In the most general setting,  $\beta \sim \mathcal{CN}(0, \eta_m)$  is a circularly symmetric complex Gaussian variable, modeling Rayleigh fading with average SNR  $\eta_m$ . The output of the matched filter becomes  $g_m \sim \mathcal{CN}(0, 1 + \eta_m)$  under  $\mathcal{H}_1$  and the test statistic follows an exponential distribution  $\Lambda_m^{\text{local}} \sim \text{Exp}(1/(1 + \eta_m))$ . Hence, the local detection probability is

$$P_{\text{D},m}^{\text{local}} = \exp\left(-\frac{\lambda_m^{\text{local}}}{1 + \eta_m}\right) \quad (4.6)$$

In terms of the local probability of false alarm,

$$P_{\text{D},m}^{\text{local}} = (P_{\text{FA},m}^{\text{local}})^{1/(1+\eta_m)} \quad (4.7)$$

### 4.3 Binary Integration

Due to the conditional independence of local decisions resulting from spatial incoherence, the global distribution under each hypothesis  $\mathcal{H}_i$  is a sum of independent but non-identically distributed random variables,

$$\delta_m \sim \text{Bernoulli}(P_m^{(i)}), \quad i \in \{0, 1\} \quad (4.8)$$

where  $P_m^{(0)} = P_{FA,m}^{\text{local}}$  and  $P_m^{(1)} = P_{D,m}^{\text{local}}$  as defined in (3.37). Then, using (3.37), the CCDF of the test statistics  $\Lambda_{\text{global}} | \mathcal{H}_i$  for both  $\Lambda_{\text{BC}}$  and  $\Lambda_{\text{WBC}}$  can be written as

$$\bar{F}_{\Lambda_{\text{global}}|\mathcal{H}_i}(\lambda^{\text{global}}) = \sum_{\Lambda_{\text{global}} \geq \lambda^{\text{global}}} \prod_{m=1}^M (P_m^{(i)})^{\delta_m} (1 - P_m^{(i)})^{1-\delta_m} \quad (4.9)$$

This expression represents a sum using all possible binary decision vectors  $\delta$ . Each configuration contributes to the CCDF if the sum  $\Lambda_{\text{global}}$  exceeds the global threshold  $\lambda^{\text{global}}$ .

Unlike the  $K$ -out-of- $M$  rule, which can produce only  $M + 1$  distinct values of  $\Lambda_{\text{BC}}$ , the weighted binary integration produces a much finer-grained distribution. In fact, the number of distinct realizable values of the test statistic  $\Lambda_{\text{WBC}}$  can rise to  $2^M$ . Therefore, evaluating the CCDF exactly requires enumerating all  $2^M$  decision vectors, which becomes computationally expensive.

Binary integration restricts the set of achievable global false alarm probabilities to a finite set. That is, for fixed local thresholds, the CCDF  $\bar{F}_{\Lambda_{\text{global}}|\mathcal{H}_0}(\cdot)$  is piecewise constant and may not align exactly with a desired global false alarm level  $P_{FA}^{\text{target}} \in (0, 1)$ . To solve this problem, we will use randomized thresholding [20].

### 4.3.1 Randomized Global Thresholding

Let  $\lambda_{\text{low}}^{\text{global}}$  be the largest possible distinct threshold smaller than  $\lambda^{\text{global}}$ . Find a unique  $\lambda^{\text{local}}$  so that

$$\bar{F}_{\Lambda_{\text{global}}|\mathcal{H}_0}(\lambda_{\text{low}}^{\text{global}}; P_{FA,\text{low}}^{\text{local}}) = P_{FA}^{\text{target}}. \quad (4.10)$$

Similarly,

$$\bar{F}_{\Lambda_{\text{global}}|\mathcal{H}_0}(\lambda^{\text{global}}; P_{FA}^{\text{local}}) = P_{FA}^{\text{target}}. \quad (4.11)$$

Both of these rules satisfy the global false alarm constraint, so their random combination also does. In practice, the FC randomly chooses between  $\lambda^{\text{global}}$  and  $\lambda_{\text{low}}^{\text{global}}$  and should accordingly communicate with receivers to determine their local false alarms as  $P_{FA}^{\text{local}}$  or  $P_{FA,\text{low}}^{\text{local}}$ . Define a randomization parameter  $q \in [0, 1)$ , which determines the probability of using the lower threshold. Then the local false alarm probability can be matched exactly to  $P_{FA,\text{desired}}^{\text{local}}$  and the randomization probability can be calculated

as follows

$$q = \frac{P_{FA,\text{desired}}^{\text{local}} - P_{FA}^{\text{local}}}{P_{FA,\text{low}}^{\text{local}} - P_{FA}^{\text{local}}}. \quad (4.12)$$

The corresponding detection probability becomes a combination of two CCDFs as

$$P_D^{\text{global}} = q \bar{F}_{\Lambda^{\text{global}}|\mathcal{H}_1}(\lambda_{\text{low}}^{\text{global}}; P_{FA,\text{low}}^{\text{local}}) + (1 - q) \bar{F}_{\Lambda^{\text{global}}|\mathcal{H}_1}(\lambda^{\text{global}}; P_{FA}^{\text{local}}). \quad (4.13)$$

This randomized approach enables fine control of the local false alarm rate while preserving the discrete nature of the test statistic.

For a  $K$ -out-of- $M$  rule,  $\lambda^{\text{global}} = K$ , and  $\lambda_{\text{low}}^{\text{global}} = K - 1$  is used, and the randomized threshold rule will be denoted with the notation  $r|K|M$ . If random thresholding is not applied, then the  $K$ -out-of- $M$  rule will be denoted without  $r$  as  $K|M$ . In addition, the effective global threshold can be calculated as

$$\lambda_{\text{eff}}^{\text{global}} = (1 - q) \lambda^{\text{global}} + q (\lambda^{\text{global}} - 1) = \lambda^{\text{global}} - q. \quad (4.14)$$

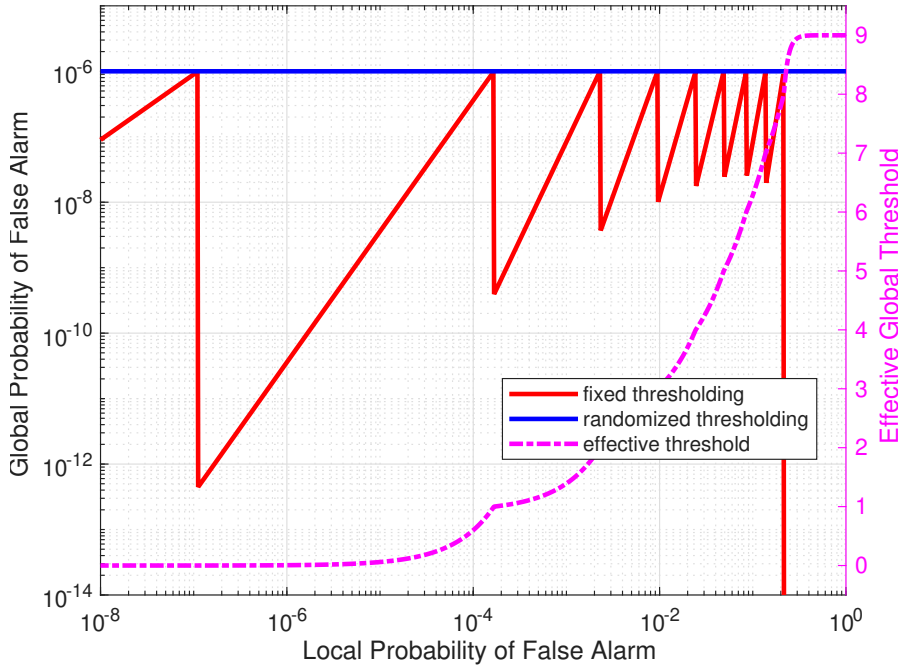


Figure 4.1:  $P_{FA}^{\text{global}}$  vs equal  $P_{FA}^{\text{local}}$  at all  $M = 9$  receiving nodes for the binary combining detector that has at least desired  $P_{FA}^{\text{global}} = 10^{-6}$ . Effective global threshold is calculated as  $\lambda_{\text{high}}^{\text{global}} - q$ .

Fig. 4.1 shows that the discrete nature of  $\lambda^{\text{global}}$  unnecessarily generates a lower  $P_{FA}^{\text{global}}$  than is desired. However, the desired  $P_{FA}^{\text{global}}$  can be satisfied by randomly choosing

$\lambda^{\text{global}}$  and  $\lambda^{\text{global}} - 1$ . Other randomization techniques can be analyzed as well, but for the purpose of this work, this randomization is sufficient.

In addition, the corresponding  $P_D^{\text{global}}$  for a spatially incoherent target is shown in Fig. 4.2. The local peaks of the  $P_D^{\text{global}}$  curves correspond to the rules without threshold randomization. Note that  $P_{FA}^{\text{local}} = 1$  means that 1 is sent to the FC in any case, which is inconsistent with the concept of distributed detection. In addition, the FC can satisfy the criterion of  $P_{FA}^{\text{global}}$  if and only if no detection is declared regardless of the received data, so  $P_D^{\text{global}}$  begins to collapse to 0 as  $P_{FA}^{\text{local}}$  increases. Fig. 4.3 has the same curves as Fig. 4.2 but its horizontal axis is not formed by logarithmically distributed values of  $P_{FA}^{\text{local}}$ , instead it has a linear axis at the cost of visual resolution for lower  $P_{FA}^{\text{local}}$ . In the following figures of this thesis, the logarithmic distribution of  $P_{FA}^{\text{local}}$  in the horizontal axis is preferred to be able to observe the effect of higher and lower values of  $P_{FA}^{\text{local}}$  at the same time.

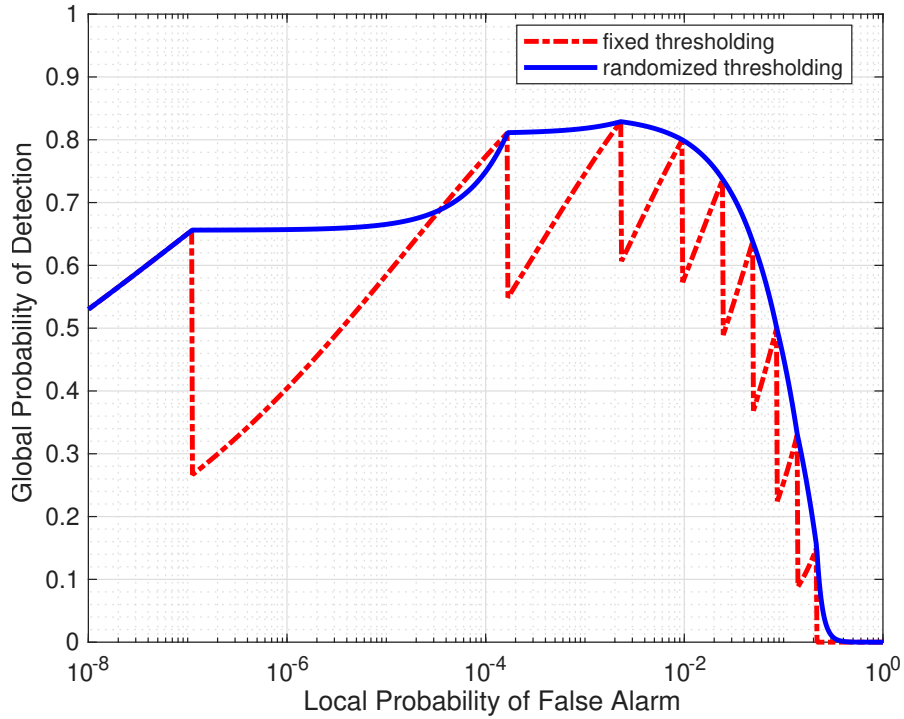


Figure 4.2:  $P_D^{\text{global}}$  vs  $P_{FA}^{\text{local}}$  of the scenario in Fig.4.1 under i.i.d. Rayleigh fluctuating with equal average SNR of  $\eta = 8$  dB at all  $M = 9$  receiving nodes.

Fig. 4.3 illustrates the linear interpolation using the 1|9 and 2|9 rules. It can be observed that fixed thresholding has a high  $P_D^{\text{global}}$  and less  $P_{FA}^{\text{global}}$ , so the randomized

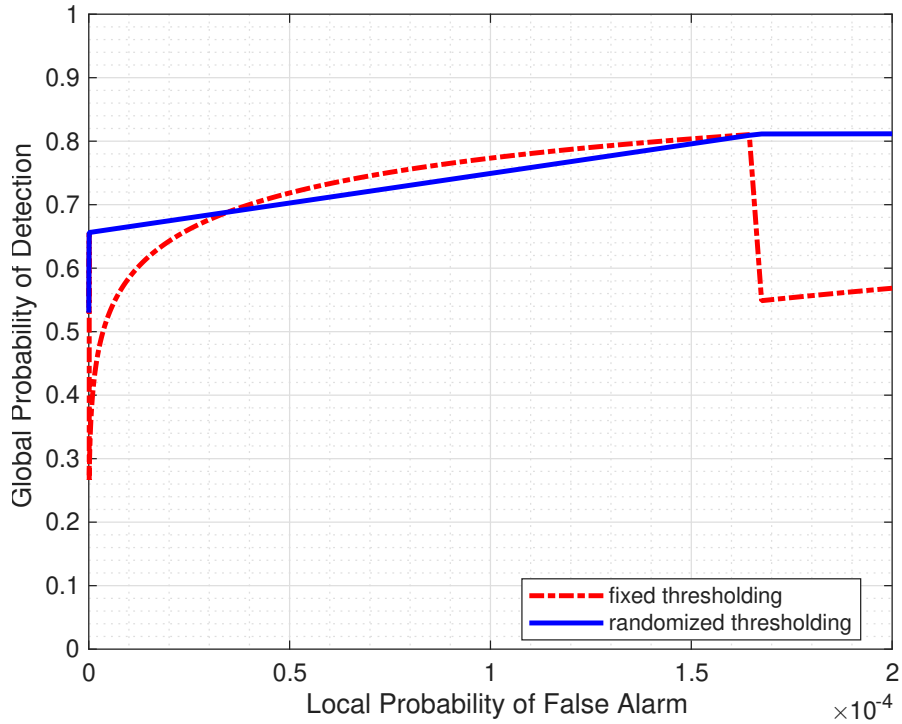


Figure 4.3:  $P_D^{\text{global}}$  vs  $P_{\text{FA}}^{\text{local}}$  of the scenario in Fig.4.1 under i.i.d. Rayleigh fluctuating with equal average SNR of  $\eta = 8$  dB at all  $M = 9$  receiving nodes.

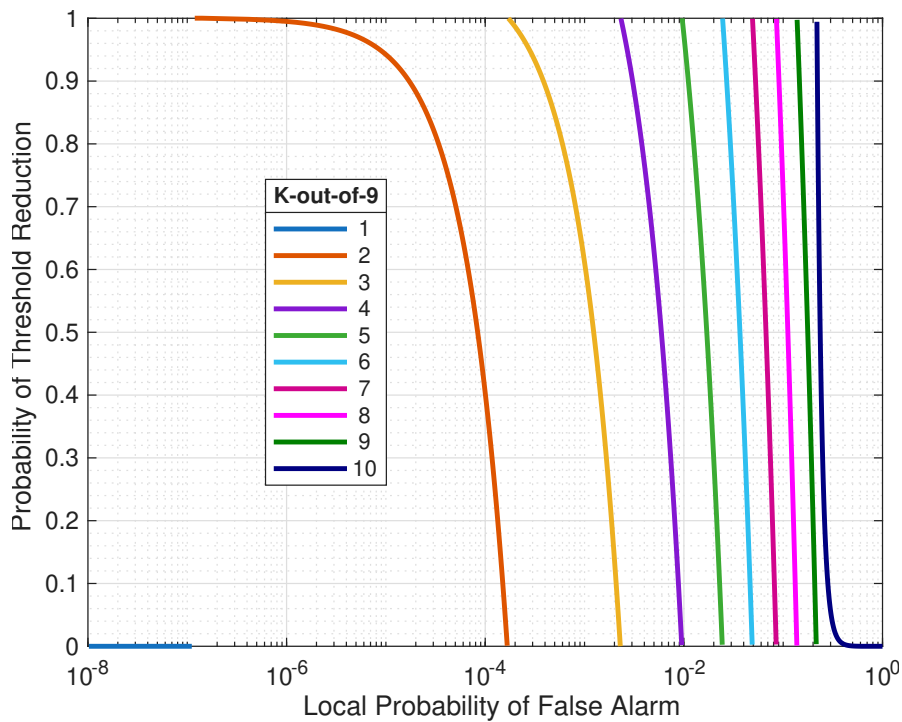


Figure 4.4: Probability  $q$  of choosing lower threshold vs  $P_{\text{FA}}^{\text{local}}$  to satisfy  $P_{\text{FA}}^{\text{global}} = 10^{-6}$  for all  $K|9$  rules.

thresholding rule is not a good idea to apply in the region from around  $0.5 \cdot 10^{-4}$  to  $1.5 \cdot 10^{-4}$ . Therefore, the randomized thresholding strategy utilized does not provide an optimal solution, but investigating the optimal rule is beyond the scope of this thesis.

Another point to pay attention to is the monotonicity of  $P_D^{\text{global}}$  vs.  $P_{\text{FA}}^{\text{local}}$  curves.  $P_D^{\text{global}}$  do not increase with increasing  $P_{\text{FA}}^{\text{local}}$  unlike the behavior  $P_D^{\text{global}}$  vs.  $P_{\text{FA}}^{\text{global}}$  because  $P_{\text{FA}}^{\text{global}}$  is fixed and therefore  $P_{\text{FA}}^{\text{local}}$  is just a parameter to adjust the optimality of the applied detection strategy.

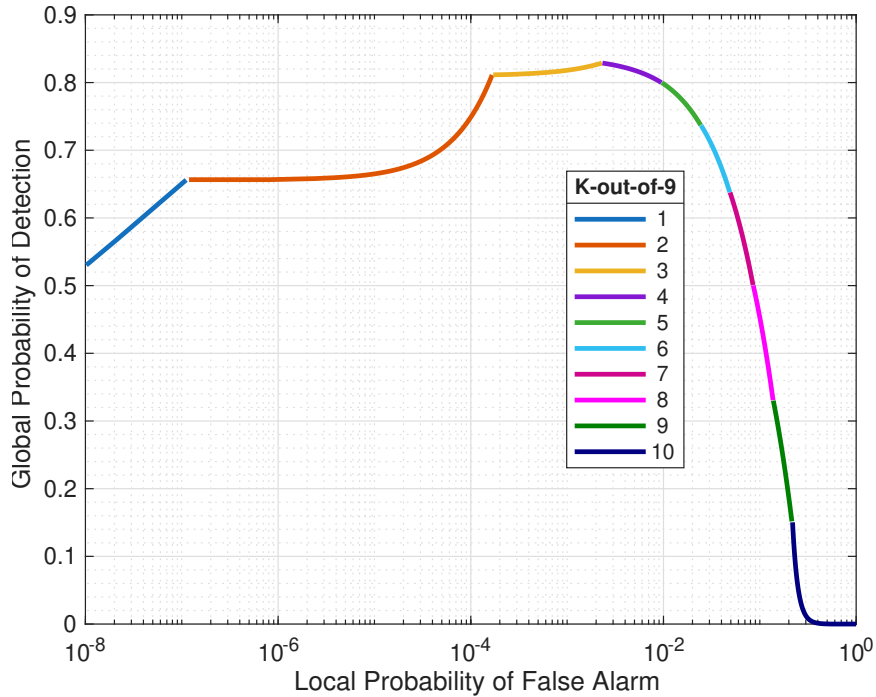


Figure 4.5:  $P_D^{\text{global}}$  vs  $P_{\text{FA}}^{\text{local}}$  under i.i.d. Rayleigh fluctuating with equal average SNR of  $\eta = 8$  dB at all  $M = 9$  receiving nodes for the BC detector that has desired  $P_{\text{FA}}^{\text{global}} = 10^{-6}$  using randomized thresholding.

### 4.3.2 Detection Performance Curves

$P_D^{\text{global}}$  curves for different number of nodes are shown in Fig. 4.6, and it can be observed that the  $K|M$  rule favors small values of  $K$  compared to  $M$  as expected for a spatially incoherent target. In fact, [12] mentions the  $1|M$  rule as the cumulative detection strategy and shows that this strategy performs best for the Swerling-2 sig-

nal model, which is analogous to the independent spatial incoherence model in the temporal domain.

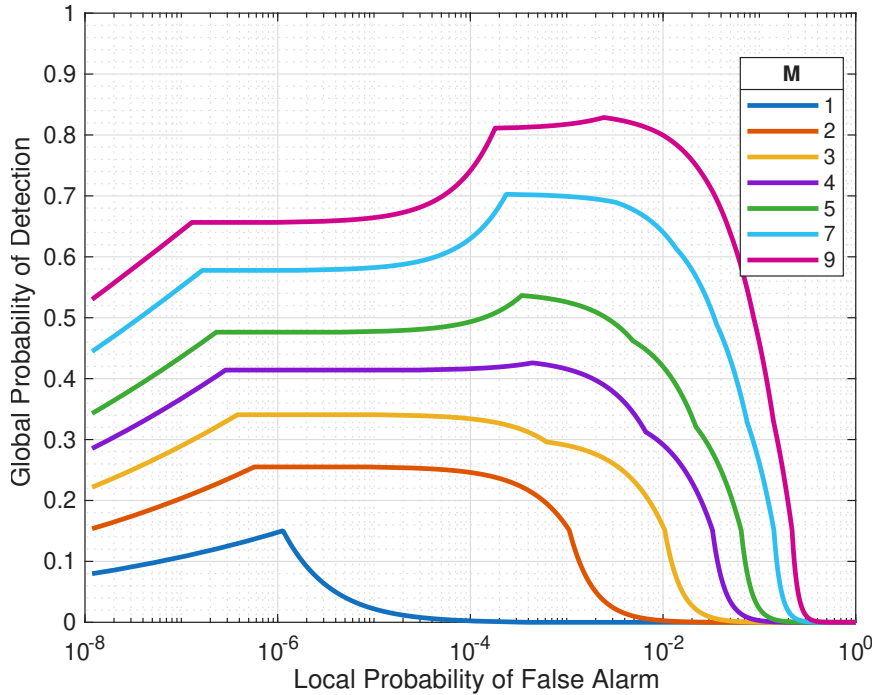


Figure 4.6:  $P_D^{\text{global}}$  vs equal  $P_{\text{FA}}^{\text{local}}$  and equal average SNR of  $\eta = 8$  dB under i.i.d. Rayleigh fluctuation at all receiving nodes for the binary combining detector that has  $P_{\text{FA}}^{\text{global}} = 10^{-6}$  with randomized thresholding.

Fig. 4.7 analyzes the detection performance under different average SNRs at the receiving nodes. To simulate a realistic detection scenario, the average SNRs were randomly generated for each receiver such that the average SNR values (in dB) were sampled as

$$\eta_{\text{dB}} = [-0.942, 3.507, 3.867, 7.556, 12.07, 2.412, 7.031, 6.928, -4.935] \quad (4.15)$$

Due to the large variation of the average SNR, the  $1|M$  rule outperforms other rules in Fig. 4.7 because a single receiving node with an average SNR of 12.07 dB has already successfully detected the target. This observation supports the idea of the cumulative detection strategy as described in [12].

In order to cover the influence of different SNR, a Monte Carlo simulation can be conducted such that the average SNR vector  $\eta_{\text{dB}}$  is realized with the magnitude square of

a independent complex Gaussian having a variance of desired reference average SNR,  $\bar{\eta}$ . In other words,  $\eta$  is generated by taking the magnitude square of the realizations of  $\mathcal{CN}(0, \bar{\eta})$ . In fact, (4.15) is one such realization for  $\bar{\eta}_{\text{dB}} = 8$ , and Fig. 4.8 shows the result for Monte Carlo simulation with 1000 different realizations and the same  $\bar{\eta}$ . Fig. 4.8 shows that the value of  $P_{\text{FA}}^{\text{local}}$  does not significantly affect the detection performance at some point around  $P_{\text{FA}}^{\text{local}} = 10^{-3}$ .

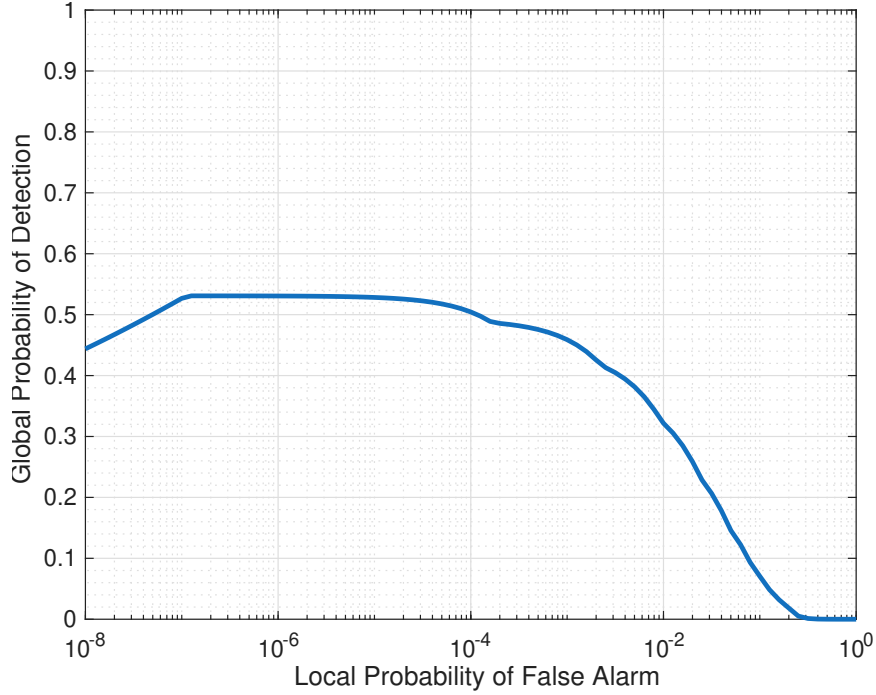


Figure 4.7:  $P_{\text{D}}^{\text{global}}$  vs  $P_{\text{FA}}^{\text{local}}$  with different average SNRs  $\eta_m$  in (4.15) under independent Rayleigh fluctuation at all  $M = 9$  receiving nodes for BC detector that has exactly  $P_{\text{FA}}^{\text{global}} = 10^{-6}$ .

#### 4.4 Distributed Noncoherent Integration

The test statistic of the weighted square law combiner (WSLC) is written in (3.42) as

$$\Lambda_{\text{WSLC}} = \sum_{m \in \mathcal{K}} \omega_m |g_m|^2. \quad (4.16)$$

Alternatively, the test statistic can be written in terms of  $T_m \sim \text{Exp}(\mu_m^{(i)})$

$$\Lambda_{\text{WSLC}} = \sum_{m \in \mathcal{K}} \omega_m (\lambda_m^{\text{local}} + T_m) = \lambda_0 + \sum_{m \in \mathcal{K}} \omega_m T_m \quad (4.17)$$

where  $\mu_m^{(0)} = 1$ ,  $\mu_m^{(1)} = 1/(1 + \eta_m)$  and the total shift is

$$\lambda_0 = \sum_{m \in \mathcal{K}} \omega_m \lambda_m^{\text{local}}. \quad (4.18)$$

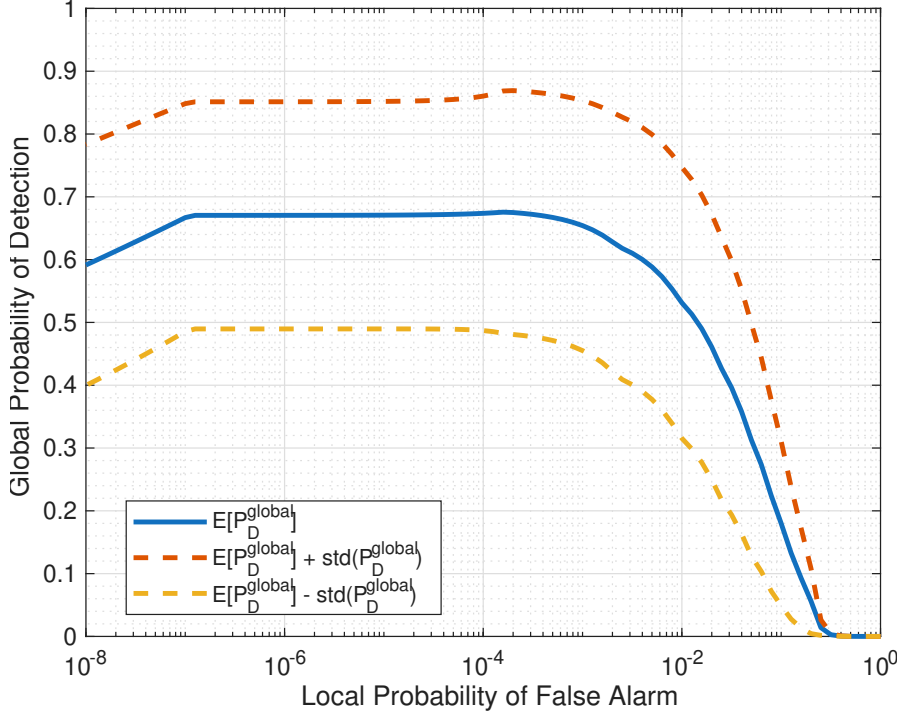


Figure 4.8:  $P_D^{\text{global}}$  vs  $P_{\text{FA}}^{\text{local}}$  with different average SNRs  $\eta_m$  realized 1000 times under independent Rayleigh fluctuation at all  $M = 9$  receiving nodes for BC detector that has exactly  $P_{\text{FA}}^{\text{global}} = 10^{-6}$ .

Let us define the rate vector as

$$\mu^{(i)} = \left[ \frac{\mu_1^{(i)}}{\omega_1}, \dots, \frac{\mu_M^{(i)}}{\omega_M} \right]_{m \in \mathcal{K}}. \quad (4.19)$$

For independently distributed complex Gaussian modeling, an expression for WSLC using matrix exponentiation is stated in the Appendix B [21]. Then the conditional CCDF becomes

$$\bar{F}_{\Lambda_{\text{WSLC}}|\mathcal{H}_i, \mathcal{K}}(\lambda^{\text{global}}) = \text{HypoExpCCDF}(\lambda^{\text{global}}; \lambda_0, \mu^{(i)}). \quad (4.20)$$

Averaging on all possible subsets of  $\mathcal{K}$ , the unconditional CCDF can be calculated as

$$\bar{F}_{\Lambda_{\text{WSLC}}|\mathcal{H}_i}(\lambda^{\text{global}}) = \sum_{\mathcal{K} \subseteq \{1, \dots, M\}} \bar{F}_{\Lambda_{\text{WSLC}}|\mathcal{H}_i, \mathcal{K}}(\lambda^{\text{global}}) \mathbb{P}(\mathcal{K} | \mathcal{H}_i). \quad (4.21)$$

Given a desired global false alarm probability  $P_{\text{FA}}^{\text{global}} \in (0, 1)$ , the global threshold  $\lambda^{\text{global}}$  is determined by solving

$$\bar{F}_{\Lambda_{\text{WSLC}}|\mathcal{H}_0}(\lambda^{\text{global}}) = P_{\text{FA}}^{\text{global}}. \quad (4.22)$$

In detection theory,  $P_{\text{FA}}^{\text{global}}$  must decrease with increasing  $\lambda^{\text{global}}$  [17]; therefore, (4.22) can be efficiently solved by numerical root-finding or grid search. Once  $\lambda^{\text{global}}$  is selected, the global detection probability is computed as

$$P_{\text{D}}^{\text{global}} = \bar{F}_{\Lambda_{\text{WSLC}}|\mathcal{H}_1}(\lambda^{\text{global}}). \quad (4.23)$$

This formulation allows for an exact analysis without Monte Carlo simulation of the detection performance as in Figures 4.9. Unlike binary integration,  $P_{\text{FA}}^{\text{local}} = 0$  corresponds to centralized noncoherent integration, and  $P_{\text{FA}}^{\text{global}}$  constraint can still be satisfied.

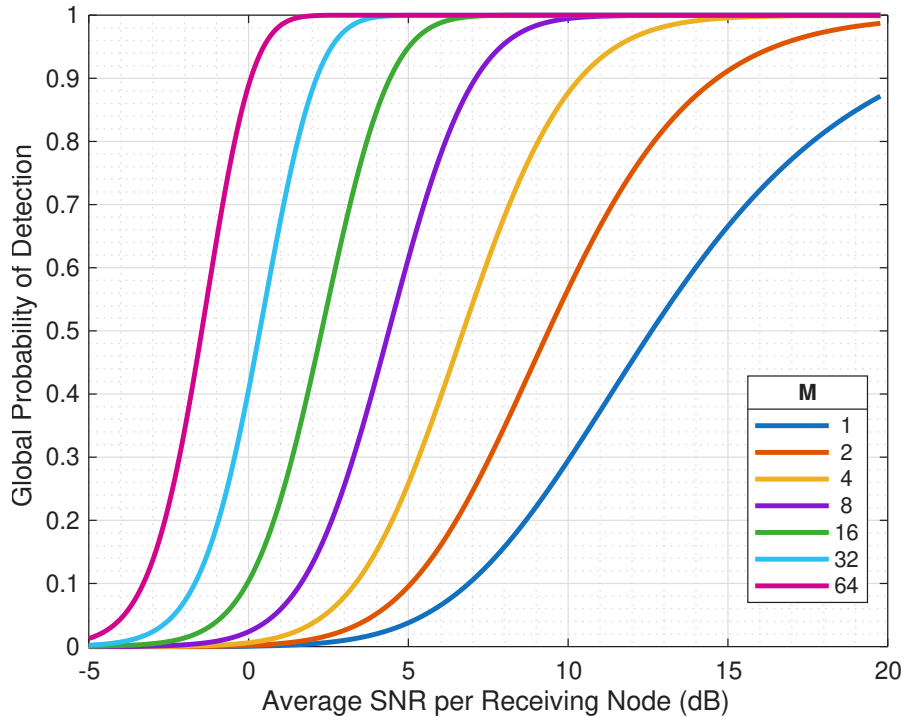


Figure 4.9:  $P_{\text{D}}^{\text{global}}$  vs equal average SNR  $\eta$  under i.i.d. Rayleigh fluctuation at different number of receiving nodes for the square law combining detector that has  $P_{\text{FA}}^{\text{global}} = 10^{-6}$  and  $P_{\text{FA}}^{\text{local}} = 1$ .

Fig. 4.9, shows the performance of the SLC without local thresholding. The detection performance increases with increasing the equal average SNR per node  $\eta$  or the

number of sensors  $M$ . The curves in the figure directly apply to the similar problem for the Swerling 2 model that has incoherence in the temporal domain.

When analyzing pulses, the average of SNR is assumed to be the same, however, it would not be realistic for a spatial scenario. Fig. 4.10 compares SLC and WSLC by scanning  $\bar{\eta}$  and shows that the performance of SLC is not very degraded compared to that of the optimal algorithm WSLC. Since WSLC requires the knowledge of average SNRs, SLC becomes a practical sub-optimum detection algorithm.

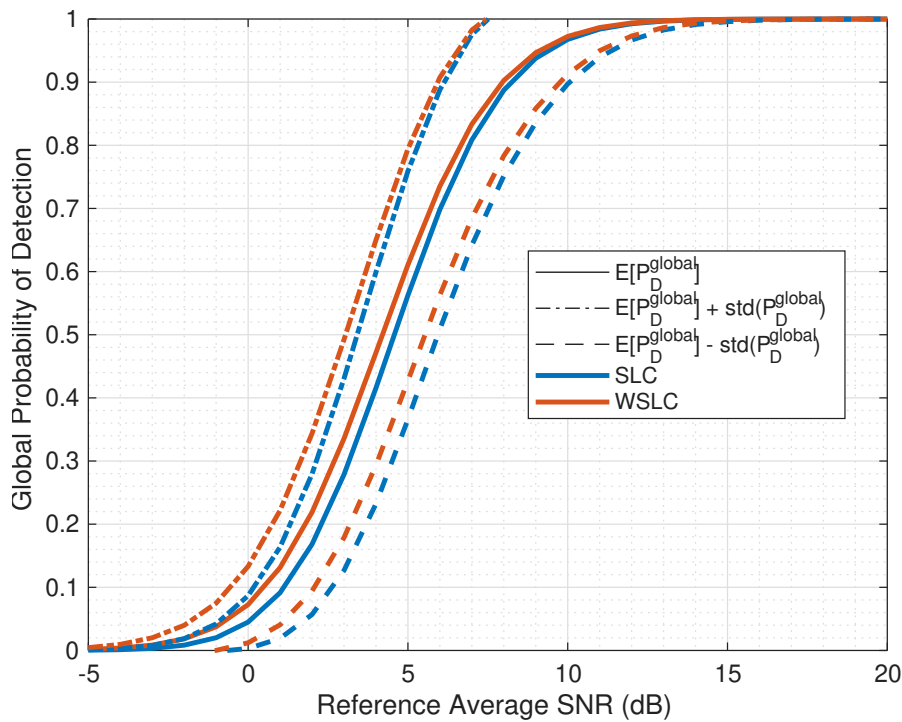


Figure 4.10:  $P_D^{\text{global}}$  vs reference average SNR  $\bar{\eta}$  under independent Rayleigh fluctuation at all  $M = 9$  receiving nodes for the SLC and WSLC detectors that have  $P_{\text{FA}}^{\text{global}} = 10^{-6}$  and  $P_{\text{FA}}^{\text{local}} = 1$ .

Fig. 4.11 presents the effect of  $P_{\text{FA}}^{\text{local}}$  on  $P_D^{\text{global}}$  for different numbers of receivers when the average SNR  $\eta = 8$  dB is equal in all receiving nodes. From the figures, the detection probability gradually decreases when the local probability of false alarm  $P_{\text{FA}}^{\text{local}}$  decreases. Unlike binary combining,  $P_{\text{FA}}^{\text{local}}$  represents the degree of centrality because  $P_{\text{FA}}^{\text{local}} = 1$  corresponds to the centralized detection and  $P_D^{\text{global}}$  has the highest value for centralized detection as expected. In addition, the SLC always performs better than BC for fixed  $P_{\text{FA}}^{\text{local}}$ , but BC with a specific  $P_{\text{FA}}^{\text{local}}$  can perform better when

$P_{FA}^{local}$  for the SLC is greatly reduced.

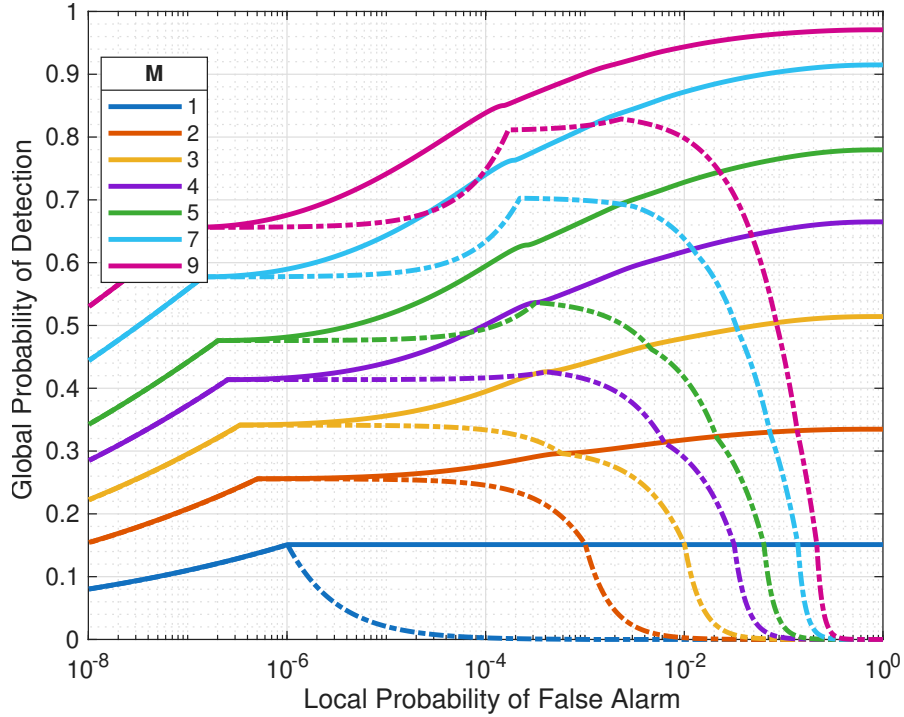


Figure 4.11:  $P_D^{global}$  vs  $P_{FA}^{local}$  with equal average SNR of  $\eta = 10$  dB under i.i.d. Rayleigh fluctuation at all receiving nodes for the unweighted SLC (solid lines) and BC (dashed lines) detectors that have  $P_{FA}^{global} = 10^{-6}$ .

Fig. 4.12 and Fig. 4.13 shows the performance of the algorithms under different average SNR at each node. The weighted SLC always performs better than the unweighted SLC and BC. The values of  $P_D^{global}$  do not vary much, so the use of weighting does not bring a significant advantage. In addition, distributed noncoherent integration always performs better than binary integration. However, the low  $P_{FA}^{local}$  region should be carefully interpreted. It may seem that BC has the same performance as the square law combiners, but at some point in the region  $P_{FA}^{local} \leq P_{FA}^{global}$ , all three algorithms coincide because all three correspond to the same algorithm so that if at least one sensor is successful in its decision, then globally the decision is declared. The coincidence point satisfies  $P_{FA}^{global} = 1 - (1 - P_{FA}^{local})^M$  and can be calculated as  $P_{FA}^{local} \approx 1.1111 \times 10^{-7}$  for this example.

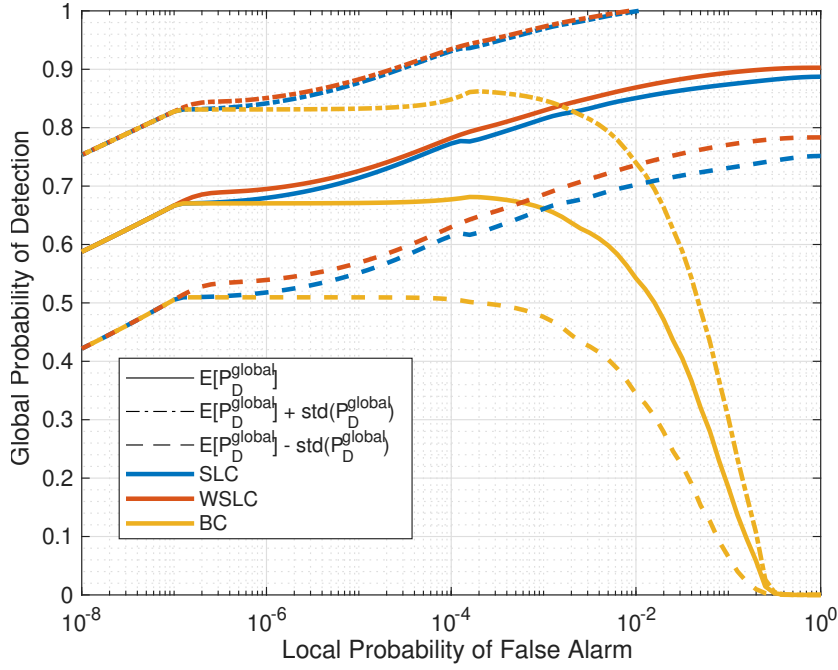


Figure 4.12:  $P_D^{\text{global}}$  vs  $P_{\text{FA}}^{\text{local}}$  with different average SNRs  $\eta_m$  realized 100 times under independent Rayleigh fluctuation at all  $M = 9$  receiving nodes for the detectors that have exactly  $P_{\text{FA}}^{\text{global}} = 10^{-6}$ .

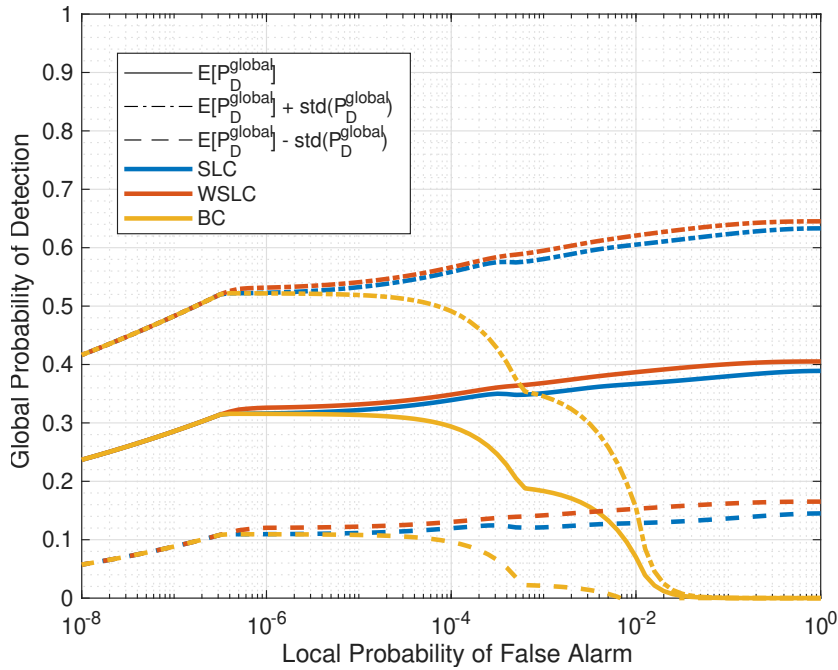


Figure 4.13:  $P_D^{\text{global}}$  vs  $P_{\text{FA}}^{\text{local}}$  with different average SNRs  $\eta_m$  realized 100 times under independent Rayleigh fluctuation at all  $M = 3$  receiving nodes for the detectors that have exactly  $P_{\text{FA}}^{\text{global}} = 10^{-6}$ .

## 4.5 Communication Performance

It is also important to provide metrics to compare algorithms in terms of communication burden. Firstly, assuming digital sampling of the received signal, a total of  $N$  temporal samples are transferred by a single node to the FC during a listening duration  $T_{RX}$ .

For centralized noncoherent detection with temporal samples represented by  $b$  bits, the data rate per interval of  $T_{RX}$  would be  $b M N$ .

For binary integration, a sequence of 0's and 1's should be transferred from the receivers to FC. The probability of 1's in this sequence of length  $N$  is equal to  $P_{FA}^{local} + N_t/N$ . Detection results are independent. Hence, the average length after optimal source coding would be roughly equal to

$$M N H_b \left( P_{FA}^{local} + \frac{N_t}{N} \right), \quad (4.24)$$

where the binary entropy function  $H_b(p) = -p \log_2(p) - (1-p) \log_2(1-p)$  [22].

For distributed noncoherent integration, both the detection indices and their power levels should be sent. The data rate for distributed detection is then  $b+1$  times the data rate of binary integration, and the data rate per interval of  $T_{RX}$  can be approximately written as

$$(b+1) M N H_b \left( P_{FA}^{local} + \frac{N_t}{N} \right). \quad (4.25)$$

In order to compare the communication rate of distributed detection with that of centralized detection, one may check the ratio

$$\frac{(b+1) M N H_b \left( P_{FA}^{local} + \frac{N_t}{N} \right)}{b M N} \approx H_b \left( P_{FA}^{local} + \frac{N_t}{N} \right). \quad (4.26)$$

Since  $P_{FA}^{local} + N_t/N \ll 1$ , and the binary entropy function's value is small and hence the communication rate is much smaller for distributed detection.

The sent data are not necessarily to be represented with large values of  $b$  bits such as 32 because it has some expected values of ranges. Firstly, it is always nonnegative and the receiver should normalize it to its noise level. In fact, it is bounded below the local threshold. Secondly, the values can be also cut from the above depending on the

number of sensors because in the worst case a target can be in the field of view of just a single node. Therefore, the upper limit should be chosen not to prevent target detection in such a case. The quantization of local test statistics is studied under the term soft fusion, where hard decision refers to binary representation with  $b = 1$ . In [23], it is shown that the 4 bit even 3 bit quantization scheme has detection performance comparable to continuous ones. As a result, the communication rate for noncoherent integration can be further reduced without degrading detection probability.

## CHAPTER 5

### SIMULATION FRAMEWORK

This chapter presents the simulation setup and methodology used to evaluate the proposed detection strategies. The simulations are built on the signal model developed in earlier chapters and are designed to reflect practical multistatic radar scenarios. An example deployment of multistatic radar will be investigated.

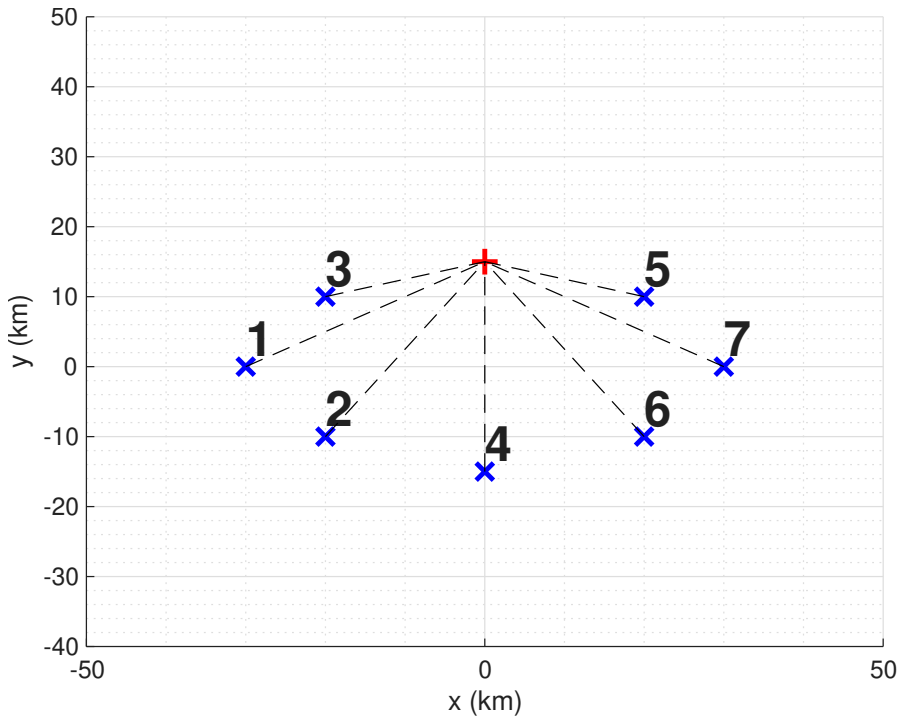


Figure 5.1: Multistatic radar scenario with 7 receiving nodes (blue crosses) and 1 transmitting node (red cross).

Fig. 5.1 shows the multistatic radar configuration in space, and the parameters of the multistatic radar network are given in Table 5.1. The direct path signals between transmitters and receivers are omitted. Both the transmitting nodes and the receiving

nodes have isotropic radiation patterns in the xy plane so that antenna gains can be thought of as along the z-direction.

Table 5.1: Simulation parameters for a multistatic radar scenario.

Parameter	Symbol	Value
Transmitted power	$P_{\text{TX}}$	40 kW
Antenna gains	$G_{\text{TX}}, G_{\text{RX}}$	$\approx 13$ dBi
Carrier frequency	$f_c$	1 GHz
Bandwidth of baseband signal	$B$	1 MHz
Bandwidth of the receivers	$B_{\text{RX}}$	1 MHz
Sampling frequencies	$f_s$	1 MHz
Pulse width	$T_{\text{PW}}$	10 $\mu\text{s}$
Pulse repetition interval	PRI	250 $\mu\text{s}$
Coherent processing interval	CPI	250 $\mu\text{s}$
Number of receiving nodes	$M$	7
Radar cross section	$\sigma_B$	1 m <sup>2</sup>
Probability of global false alarm	$P_{\text{FA}}^{\text{global}}$	10 <sup>-6</sup>

The region of interest is divided into cells as described in Section 3.2. The size of the cells is chosen considering the minimum possible resolution of  $c/2B \approx 150\text{m}$  in (2.18). For each cell, noncoherent integration takes place using the corresponding matched filter sample as in (3.3). There is a single target in the scene and it is located at  $\mathbf{p}_T = [10.2, -15.1, 0]^T$  km with an RCS of  $\sigma_B = 1 \text{ m}^2$ . The target is perfectly located at the center of one of the cells. Fig. 5.2 shows the result of centralized noncoherent integration in each cell assigned to the xy plane.

In Section 4.4, it was shown that a wide range of  $P_{\text{FA}}^{\text{local}}$  degrades  $P_{\text{D}}^{\text{global}}$  to an acceptable level under the independent Rayleigh fluctuations for distributed noncoherent integration. From the performance curves,  $P_{\text{FA}}^{\text{local}} = 10^{-2}$  can be chosen without a great loss in detection performance. In addition, the multistatic radar network collects a total of  $N = 250$  samples per node, therefore  $P_{\text{FA}}^{\text{local}} < 1/250$  will not further reduce the data rate as discussed in 4.5.

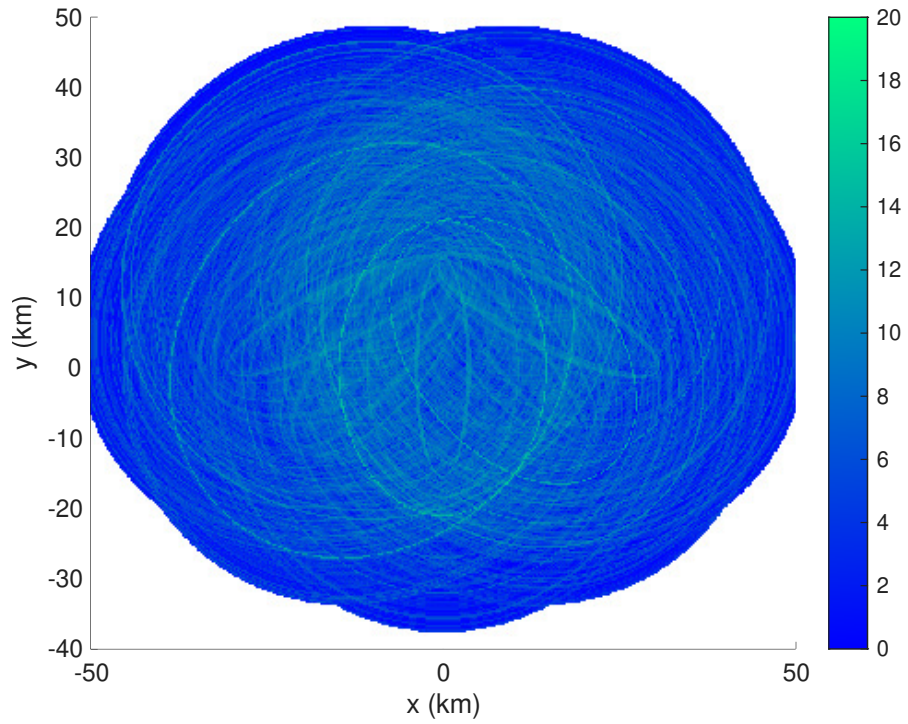


Figure 5.2: The output of the centralized noncoherent integration applied to each CUT. Power scale is in terms of dB.

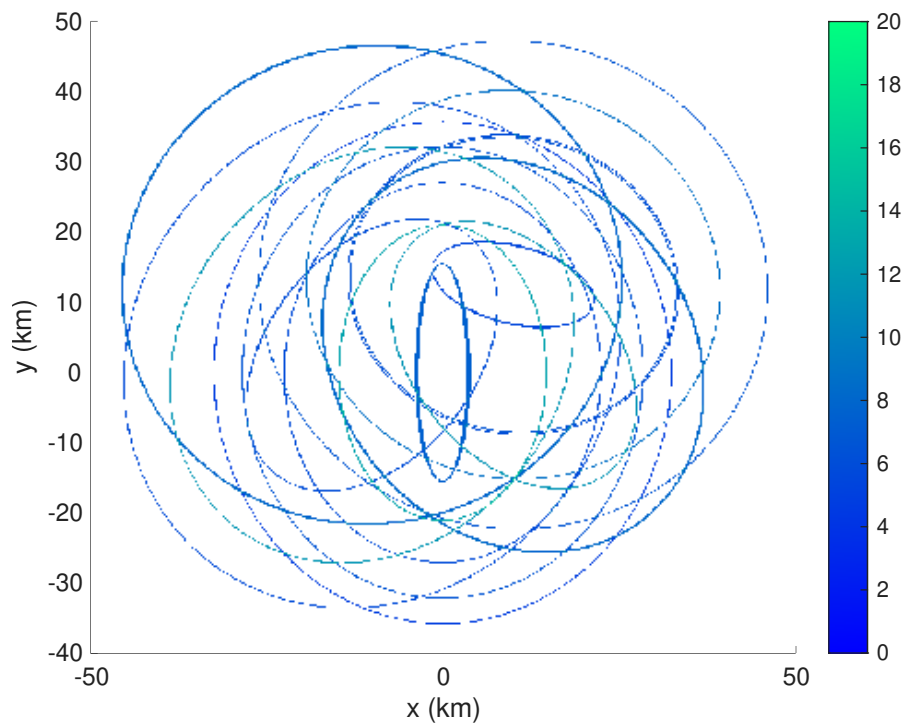


Figure 5.3: The output of the distributed noncoherent integration with  $P_{FA}^{local} = 10^{-2}$  applied to each CUT. Power scale is in terms of dB.

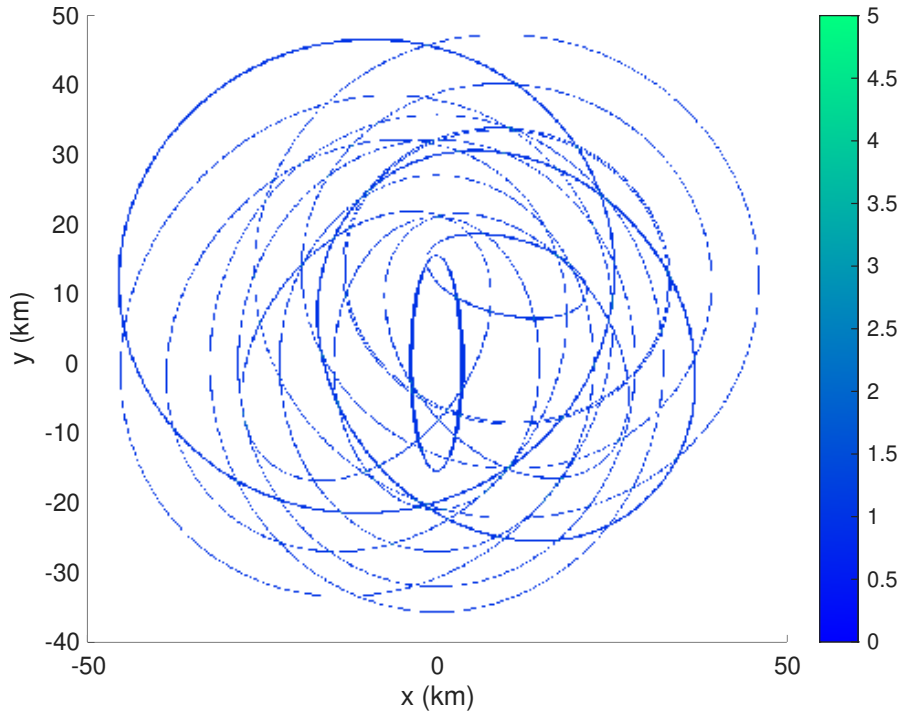


Figure 5.4: The integer output of the binary integration with  $P_{FA}^{local} = 10^{-2}$  applied to each CUT.

Fig. 5.2 shows the created target response map by applying centralized noncoherent integration. For each cell, all associated matched filter outputs are integrated. If local thresholding is applied, the result in Fig. 5.2 is created only using cells that have at least 1 contributing receiving node that has declared a target locally. Fig. 5.3 shows the cleaning of the spatial image thanks to local thresholding with  $P_{FA}^{local}$ . In this figure, the ellipses correspond to the same delay value; hence, all cells on these ellipses utilize the same matched filter output for the same amount of delay. Local thresholding also decreases the number of probed cells, which helps to relax the computational resources of the FC. Finally, Fig. 5.4 illustrates the result of binary integration which has a similar result to that of distributed noncoherent integration.

For the random trial utilized, the three detection algorithms peaked at the correct target location. However, there are other cells that exceed  $\lambda^{global}$  formed because of constant time delay ellipses of power dominant receivers. In addition, there may be more than one target in the region of interest, but the peak location just indicates a single target. Therefore, cell search methods such as in [24] can be utilized for

the detection of multiple targets. The cell search method utilizes the behavior of neighboring cells that may be useful for target detection.

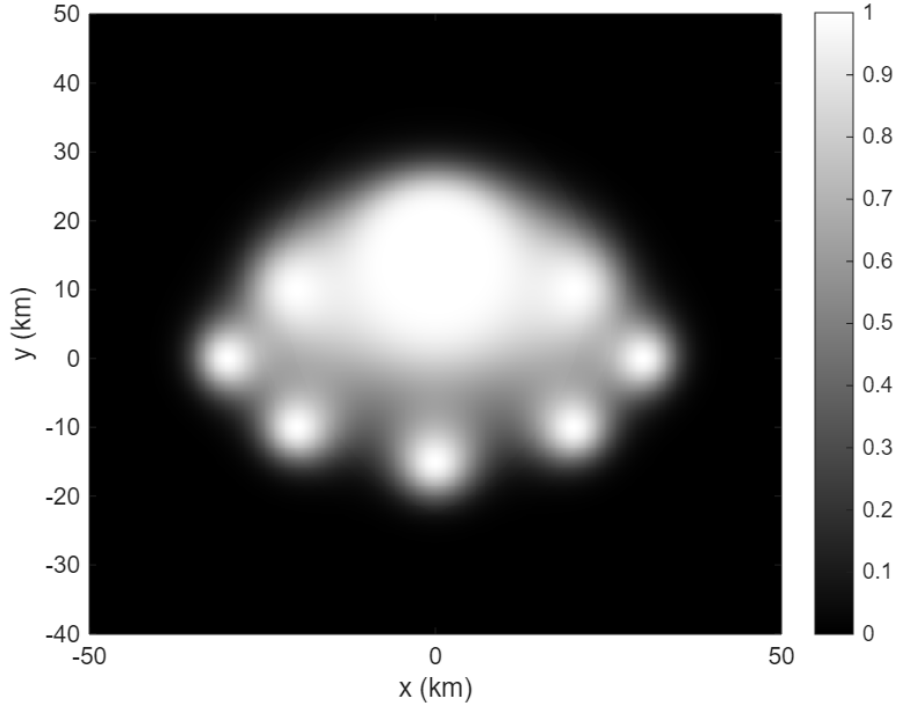


Figure 5.5: Coverage of the multistatic radar configuration for centralized noncoherent integration assuming a single target with RCS  $\sigma_B = 1 \text{ m}^2$ .

The coverage of the multistatic radar network can be calculated in this specific configuration in terms of probability of detection. The coverage figures are generated without the need for a Monte Carlo simulation owing to analytical expressions. They are evaluated directly from expected average SNR values; therefore, resolution effects are not included in these results. The expected average SNRs are calculated using the radar range equation and the matched filtering gain with the straddle loss as discussed in Chapter 2.

The following figures show the coverage map created by looking at every cell and finding the corresponding  $P_D^{\text{global}}$ . Figures 5.5 to 5.8, illustrate the probability of detection in the  $xy$  plane for a target having RCS  $\sigma_B = 1 \text{ m}^2$ .

For binary integration, there are two coverage figures. Fig. 5.7 is created for very low  $P_{\text{FA}}^{\text{local}}$  of  $1.4 \cdot 10^{-7}$  because it corresponds to the  $1|M$  rule and it has the best performance for especially regions with different average SNRs. For  $1|M$  rule,  $P_{\text{FA}}^{\text{local}}$

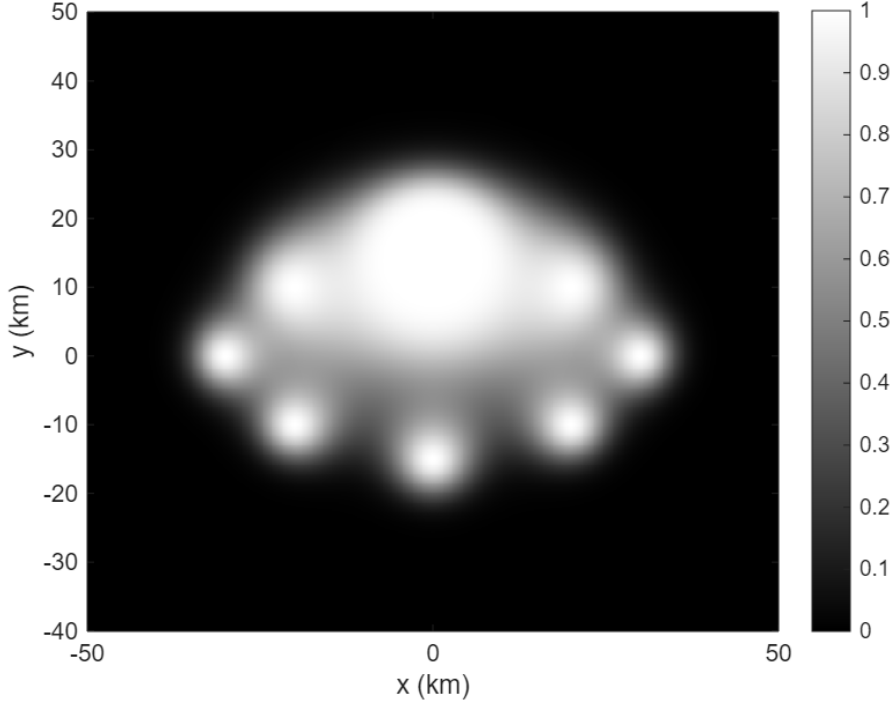


Figure 5.6: Coverage of the multistatic radar configuration for distributed noncoherent integration assuming a single target with RCS  $\sigma_B = 1 \text{ m}^2$  for  $P_{\text{FA}}^{\text{local}} = 10^{-2}$ .

can be calculated as  $\approx 1.429 \times 10^{-7}$  using the CCDF as  $P_{\text{FA}}^{\text{global}} = 1 - (1 - P_{\text{FA}}^{\text{local}})^M$ .

However, it is possible to improve target detection performance for regions that have similar average SNRs. For this reason, Fig. 5.8 is created with  $P_{\text{FA}}^{\text{local}} = 1.9 \cdot 10^{-4}$  and has better performance in such regions.

From the coverage figures, constant contours of  $P_{\text{D}}^{\text{global}}$  can be compared between algorithms. Fig. 5.9 is the constant contour  $P_{\text{D}}^{\text{global}} = 0.85$ , and as expected, centralized detection has the widest coverage, and binary detection has the smallest one. Similarly, Fig. 5.10 illustrates constant contours  $P_{\text{D}}^{\text{global}} = 0.70$ . The coverage for distributed noncoherent integration is very close to the coverage of centralized detection compared to binary integration, but the data rate of distributed noncoherent integration is greater than by a factor of  $b + 1$  bits compared to binary integration.

In the figures of constant contours of  $P_{\text{D}}^{\text{global}}$ , there are 3 curves for binary combining. Since  $P_{\text{FA}}^{\text{local}} = 10^{-2}$  is used for distributed SLC, it would not be fair to take directly  $P_{\text{FA}}^{\text{local}} = 10^{-2}$  for BC because it is possible that BC performs better with a lower  $P_{\text{FA}}^{\text{local}}$

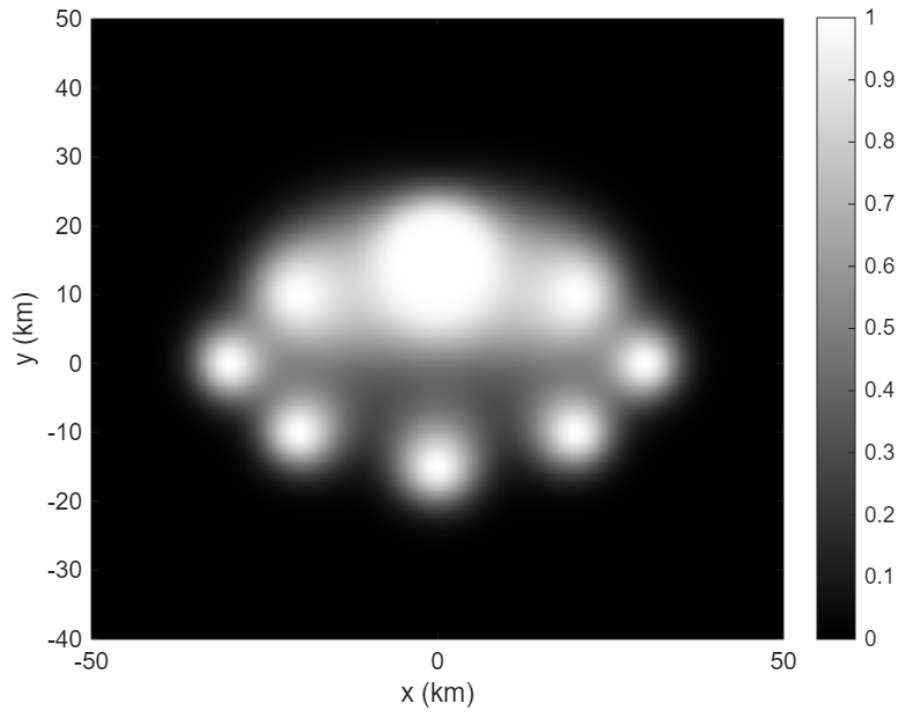


Figure 5.7: Coverage of the multistatic radar configuration for binary integration assuming a single target with RCS  $\sigma_B = 1 \text{ m}^2$  for  $P_{\text{FA}}^{\text{local}} = 1.4 \cdot 10^{-7}$ .

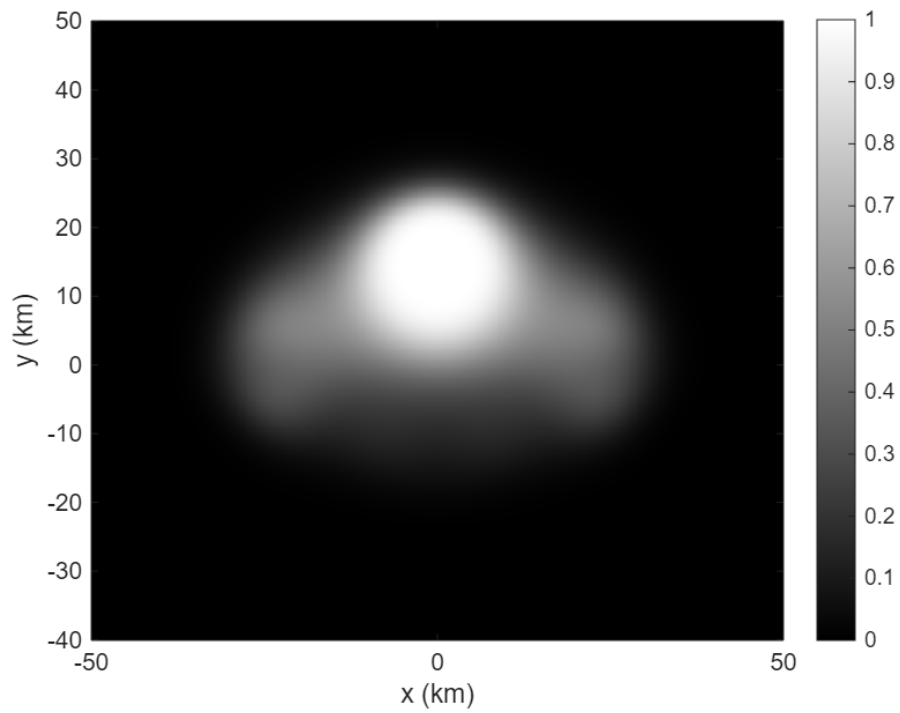


Figure 5.8: Coverage of the multistatic radar configuration for binary integration assuming a single target with RCS  $\sigma_B = 1 \text{ m}^2$  for  $P_{\text{FA}}^{\text{local}} = 1.9 \cdot 10^{-4}$ .

as observed in Section 4.4. Therefore, 100 values of  $P_{FA}^{local}$  are scanned between  $10^0$  and  $10^{-8}$  to find the maximum and minimum possible coverage of BC. It turns out that the  $1|M$  rule provides the largest coverage, which means that if at least 1 sensor declares detection, then it is enough to declare target detection globally. Even if this coverage is not big as that of distributed noncoherent integration, it provides an acceptable coverage. From these results, the  $1|M$  rule could be a suitable choice for the multistatic target detection algorithm, however, we were not interested in the target parameters, but the sent power values would be useful for cell search methods. For example, false detection of targets in other cells increases because it will be enough to detect a target even if the FC produces the sum with a value of 1. Therefore, there will be many cells that have the fusion result of 1 and this will make it difficult to eliminate detections from these cells that contain the part of the response of the real target, so the problem of reducing detection of ghosts of targets will be challenging.

Also, the ratio between data rates of binary integration and distributed noncoherent integration is just the number of bits. Even, it is possible that binary results are sent to FC together with other information so that the data rates of these integration techniques become very close. In short, the utilization of distributed noncoherent integration provides advantages for target detection and parameter estimation under an acceptable level of data rate increase.

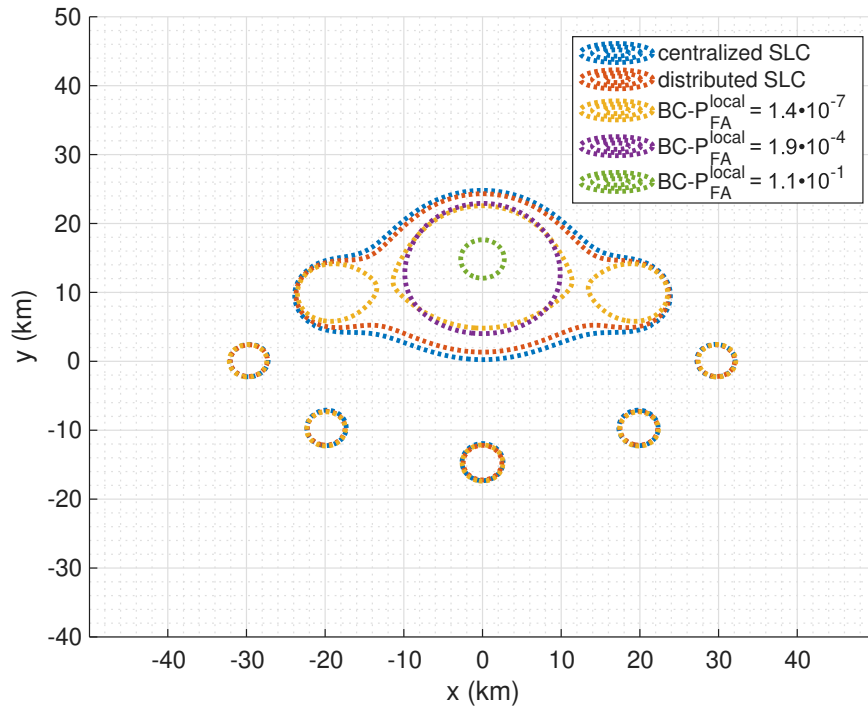


Figure 5.9:  $P_D^{\text{global}} = 0.85$  contours for the coverage of the multistatic radar configuration assuming a single target with RCS  $\sigma_B = 1 \text{ m}^2$ .

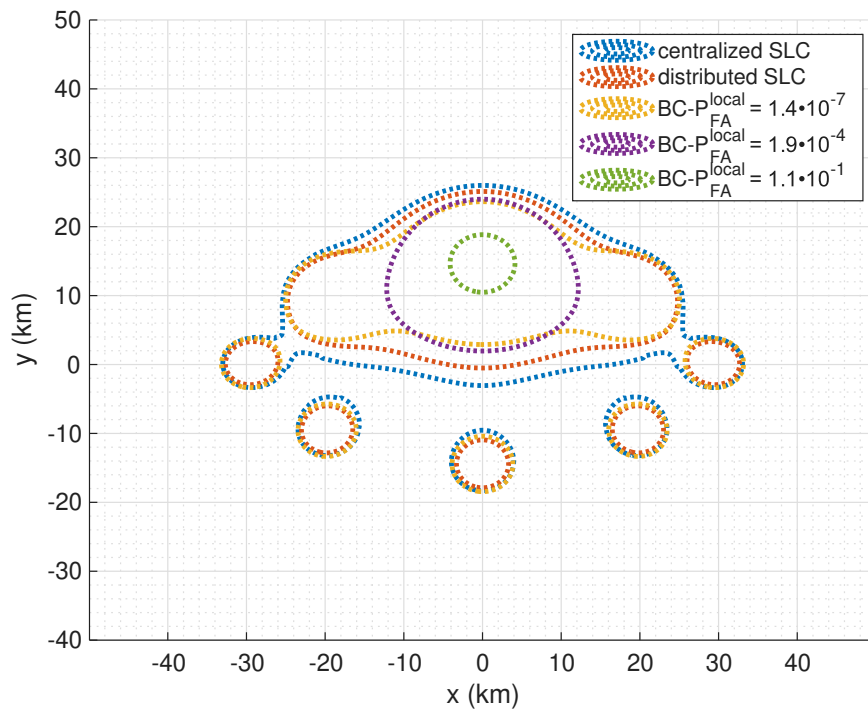


Figure 5.10:  $P_D^{\text{global}} = 0.70$  contours for the coverage of the multistatic radar configuration assuming a single target with RCS  $\sigma_B = 1 \text{ m}^2$ .



## CHAPTER 6

### CONCLUSIONS

This thesis investigated target detection in multistatic radar networks, with a particular focus on noncoherent integration and compared centralized and distributed detection architectures. The work began with radar fundamentals, mainly on how target parameters behave in multistatic setups. These fundamentals set the scene for the limitations we face in multistatic radars. From there, the thesis moved on to modeling how the received signal can vary across nodes, mainly due to changes in reflectivity or mismatches in timing and synchronization. These models made it possible to examine different cases of coherent and noncoherent processing, depending on what information about phase and amplitude was available.

A cell-based target detection scheme is defined and centralized detection algorithms are presented. Based on these detection models, the thesis then addressed distributed architectures in which local receivers apply thresholding and send only limited information to a central fusion point. Both binary integration and distributed noncoherent integration were investigated. Theoretical derivations of false alarm and detection probabilities were provided under various data combining rules. In addition, binary integration with random thresholding is proposed to match the global false alarm with a fixed local false alarm rate. The relationship between the local false alarm rate and the communication rate is also demonstrated.

Finally, simulations were carried out for a practical multistatic radar to see the effect of local thresholding. Local thresholding also brings an advantage in computational resources as the number of probed cells decreases. In addition, binary integration and distributed noncoherent integration schemes are compared in terms of multistatic radar coverage. It is observed that distributed noncoherent integration is an alternative

for centralized detection and binary integration because of its reduced communication rate and detection performance comparable to that of optimal centralized detection. In addition, sent power values of distributed noncoherent integration can be beneficial for estimating target parameters and reducing ghost target detections due to target responses at other cells compared to binary integration.

Binary integration with the OR rule offers the largest multistatic radar coverage among binary integration rules, mainly due to independent and non-identical returns. However, binary rules with higher thresholds are more beneficial for target localization because wrong associations due to extra intersection points are less likely to occur. Therefore, smooth power values of distributed noncoherent integration have a further advantage over binary integration. The main disadvantage is an increased communication rate, but the entire multistatic network can be designed to account for this trade-off.

In conclusion, this thesis contributes to a comprehensive statistical framework for detection in multistatic radar systems and provides the following key outcomes:

- Centralized and distributed architectures for noncoherent detection are systematically modeled and compared.
- Binary integration with random thresholding is introduced to align global and local false alarm rates while analyzing its effect on communication.
- Distributed noncoherent integration is shown to provide comparable detection to centralized schemes with reduced communication and added benefits for parameter estimation and ghost target reduction.

## 6.1 Future Works

The findings of this thesis can be extended to several topics:

- **Hardware validation:** Performance metrics under real-world hardware constraints such as latency, quantization, and synchronization errors can be investigated.

- **Multi-target detection:** Advanced algorithms can be designed to detect multiple targets from the generated response map using SRCs. Reduction of ghost-target detection can be investigated. In addition, the estimation of target parameters and performance metrics can be studied.



## REFERENCES

- [1] E. Fishler, A. Haimovich, R. Blum, L. Cimini, D. Chizhik, and R. Valenzuela, “Spatial diversity in radars—models and detection performance,” *IEEE Transactions on Signal Processing*, vol. 54, pp. 823–838, March 2006.
- [2] S. Zhou, H. Liu, Y. Zhao, and L. Hu, “Target spatial and frequency scattering diversity property for diversity mimo radar,” *Signal Processing*, vol. 91, no. 2, pp. 269–276, 2011.
- [3] V. Chernyak, *Fundamentals of Multisite Radar Systems: Multistatic Radars and Multistatic Radar Systems*. London: Routledge, first edition ed., 1998.
- [4] Y. Teng, *Fundamental aspects of netted radar performance*. Thesis (doctoral), University of London, University College London (United Kingdom), 2010.
- [5] S. R. Doughty, *Development and performance evaluation of a multistatic radar system*. Thesis (doctoral), University of London, University College London (United Kingdom), 2008.
- [6] P. Stoica and J. Li, *MIMO Radar Signal Processing*. Hoboken, New Jersey: J. Wiley & Sons, 2015.
- [7] M. A. Richards, *Fundamentals of Radar Signal Processing*. New York: McGraw-Hill Education, second edition ed., 2014.
- [8] C. J. Bradley, P. J. Collins, D. G. Falconer, J. Fortuny-Guasch, and A. J. Terzuoli, “Evaluation of a near-field monostatic-to-bistatic equivalence theorem,” *IEEE Transactions on Geoscience and Remote Sensing*, vol. 46, pp. 449–457, Feb 2008.
- [9] H. Buddendick and T. Eibert, “Concept for accelerated ray-based monostatic rcs simulations using bistatic approximations,” *Advances in Radio Science - Kleinheubacher Berichte*, vol. 7, 05 2009.

- [10] F. T. Bette, T. M. Gemmer, S. v. Wnuck-Lipinski, H. Bartko, B. Derat, S. Otto, M. Willemsen, and W. Keusgen, "Monostatic measurement setup and transformation method to obtain bistatic reflection patterns of reconfigurable intelligent surfaces," in *2024 Antenna Measurement Techniques Association Symposium (AMTA)*, pp. 1–6, Oct 2024.
- [11] A. De Luca, *Forward scatter radar: innovative configurations and studies*. Thesis (doctoral), University of Birmingham, 2018.
- [12] P. S. Diao, T. Alves, B. Poussot, and S. Azarian, "A review of radar detection fundamentals," *IEEE Aerospace and Electronic Systems Magazine*, vol. 39, pp. 4–24, Sep. 2024.
- [13] Q. Zou, Z. Behdad, O. Tugfe Demir, and C. Cavdar, "Distributed versus centralized sensing in cell-free massive mimo," *IEEE Wireless Communications Letters*, vol. 13, pp. 3345–3349, Dec 2024.
- [14] Y. Yang, H. Su, Q. Hu, S. Zhou, and J. Huang, "Spatial resolution cell based centralized target detection in multistatic radar," *Signal Processing*, vol. 152, pp. 238–246, 2018.
- [15] M. Mandlik and Z. Nemeč, "An accuracy synchronization method for passive radar system," in *2014 24th International Conference Radioelektronika*, pp. 1–4, April 2014.
- [16] Z. Zhang, Y. Zhou, S. Zhang, S. Shang, T. You, and L. Zhang, "Elliptical spatial resolution cell-based centralized target detection in multistatic radar," *IEEE Sensors Journal*, vol. 24, pp. 15367–15377, May 2024.
- [17] H. L. V. Trees, *Detection, Estimation, and Modulation Theory, Part I: Detection, Estimation, and Linear Modulation Theory*. J. Wiley & Sons, 2001.
- [18] Z. Chair and P. Varshney, "Optimal data fusion in multiple sensor detection systems," *IEEE Transactions on Aerospace and Electronic Systems*, vol. AES-22, pp. 98–101, Jan 1986.
- [19] G. Verma, V. Dhage, and S. S. Chauhan, "Analysis of combined data-decision fusion scheme for cognitive radio networks," in *2018 2nd International Conference on Inventive Systems and Control (ICISC)*, pp. 1324–1327, Jan 2018.

- [20] W. Dong and M. Kam, “Dependent randomization in parallel binary decision fusion,” *IEEE/CAA Journal of Automatica Sinica*, vol. 8, pp. 361–376, February 2021.
- [21] B. Legros and O. Jouini, “A linear algebraic approach for the computation of sums of erlang random variables,” *Applied Mathematical Modelling*, vol. 39, no. 16, pp. 4971–4977, 2015.
- [22] J. A. T. Thomas M. Cover, *Elements of Information Theory*. J. Wiley & Sons, second edition ed., 2005.
- [23] J. Luo and X. He, “A soft–hard combination decision fusion scheme for a clustered distributed detection system with multiple sensors,” *Sensors*, vol. 18, p. 4370, 12 2018.
- [24] Z. Zhang, Y. Zhou, S. Shang, L. Zhang, and L. Du, “Sparse cell search method for centralized target detection in multistatic radar,” *IEEE Transactions on Aerospace and Electronic Systems*, vol. 61, pp. 10229–10242, Aug 2025.



## Appendix A

### CONDITIONAL LIKELIHOOD RATIO

This section derives the LRT of  $\mathbf{y}^{(j)}$  in Equation (3.12) for a given  $\mathbf{h}$ . Throughout this appendix,  $\mathbf{y}^{(j)}$  is simply written as  $\mathbf{y}$ . Under  $\mathcal{H}_0$ ,  $\mathbf{y}$  is distributed as  $\mathbf{y} \sim \mathcal{CN}(\mathbf{0}, \Sigma)$  due to independently distributed noisy observations, then the conditional probability becomes

$$p(\mathbf{y} | \mathcal{H}_0) = \frac{1}{\pi^M \det \Sigma} \exp(-\mathbf{y} \Sigma^{-1} \mathbf{y}^\dagger). \quad (\text{A.1})$$

Under  $\mathcal{H}_1$ ,  $\mathbf{y}$  has a non-zero mean  $\mathbf{h}$ , so  $\mathbf{y} \sim \mathcal{CN}(\mathbf{h}, \Sigma)$ , and the conditional probability is

$$p(\mathbf{y} | \mathcal{H}_1, \mathbf{h}) = \frac{1}{\pi^M \det \Sigma} \exp(-(\mathbf{y} - \mathbf{h}) \Sigma^{-1} (\mathbf{y} - \mathbf{h})^\dagger) \quad (\text{A.2})$$

It is simpler to work with log-likelihood ratio (LLR) instead of likelihood ratio because the product becomes the sum. Applying logarithm makes a monotonic transformation; hence do not affect the optimality of the test. Then, the log-likelihood ratio conditioned on  $\mathbf{h}$  is

$$\ln \Lambda(\mathbf{y} | \mathbf{h}) = \ln \frac{f(\mathbf{y} | \mathcal{H}_1)}{f(\mathbf{y} | \mathcal{H}_0)} = -(\mathbf{y} - \mathbf{h}) \Sigma^{-1} (\mathbf{y} - \mathbf{h})^\dagger + \mathbf{y} \Sigma^{-1} \mathbf{y}^\dagger. \quad (\text{A.3})$$

After the expansion of the first term and simplification, LLR expression becomes

$$\ln \Lambda(\mathbf{y} | \mathbf{h}) = \mathbf{y} \Sigma^{-1} \mathbf{h}^\dagger + \mathbf{h} \Sigma^{-1} \mathbf{y}^\dagger - \mathbf{h} \Sigma^{-1} \mathbf{h}^\dagger. \quad (\text{A.4})$$

The first two terms are complex conjugates of each other; hence, the conditional log-likelihood ratio can be equivalently expressed compactly as

$$\ln \Lambda(\mathbf{y} | \mathbf{h}) = 2\Re \{ \mathbf{h}^\dagger \Sigma^{-1} \mathbf{y} \} - \mathbf{h}^\dagger \Sigma^{-1} \mathbf{h}. \quad (\text{A.5})$$

This expression is the test statistics of the LLR under known spatial noise covariance  $\Sigma$  and known spatial gain vector  $\mathbf{h}$ .



## Appendix B

### DISTRIBUTION OF A SUM OF SHIFTED EXPONENTIAL RANDOM VARIABLES

Let  $T_1, T_2, \dots, T_K$  be independent exponential random variables with non-identical rate parameters  $\mu_1, \mu_2, \dots, \mu_K$ , such that

$$T_m \sim \text{Exp}(\mu_m), \quad \text{for } m = 1, \dots, K. \quad (\text{B.1})$$

Additionally, let each variable be shifted by a known deterministic constant  $\lambda_m \geq 0$ . Form the total shifted sum as

$$\Lambda \triangleq \sum_{m=1}^K (\lambda_m + T_m) = \lambda_0 + \sum_{m=1}^K T_m, \quad \lambda_0 \triangleq \sum_{m=1}^K \lambda_m. \quad (\text{B.2})$$

In order to formulate the CCDF, let us define the generator matrix  $\mathbf{M} \in \mathbb{R}^{K \times K}$  as

$$\mathbf{M} = \begin{bmatrix} -\mu_1 & \mu_1 & 0 & \cdots & 0 \\ 0 & -\mu_2 & \mu_2 & \cdots & 0 \\ \vdots & \ddots & \ddots & \ddots & \vdots \\ 0 & \cdots & 0 & -\mu_{K-1} & \mu_{K-1} \\ 0 & \cdots & 0 & 0 & -\mu_K \end{bmatrix}. \quad (\text{B.3})$$

Let  $\mathbf{j} = [1 \ 0 \ \cdots \ 0]^T \in \mathbb{R}^{K \times 1}$  be the initial state vector and let  $\mathbf{1} \in \mathbb{R}^{K \times 1}$  be the vector filled with all ones. Then the CCDF of  $\Lambda$  is given by

$$\bar{F}_\Lambda(\lambda) = \mathbf{j}^T \exp(\mathbf{M}(\lambda - \lambda_0)_+) \mathbf{1} \quad (\text{B.4})$$

where  $(\cdot)_+ = \max\{\cdot, 0\}$ , and  $\exp(\cdot)$  is the matrix exponentiation, not an element-wise operation. Let us define a short hand notation as

$$\text{HypoExpCCDF}(\lambda; \lambda_0, \mu) \triangleq \mathbf{j}^T \exp(\mathbf{M}(\lambda - \lambda_0)_+) \mathbf{1} \quad (\text{B.5})$$

where  $\mu = [\mu_1, \mu_2, \dots, \mu_K]^\top$  denotes the rate vector. This function is referenced in Section 3.5.2 when expressing the conditional distribution of test statistics involving truncated exponentially distributed random variables.

- **Special Case: Identical Rates (Erlang Distribution)**

If  $\mu_m = \mu$  for all  $m$ , then  $\sum T_m \sim \text{Erlang}(K, \mu)$ , and the CCDF reduces to

$$\bar{F}_\Lambda(\lambda) = \bar{\Gamma}(K, \mu(\lambda - \lambda_0)_+) \quad (\text{B.6})$$

where  $\bar{\Gamma}(k, x)$  denotes the regularized upper incomplete gamma function

$$\bar{\Gamma}(k, x) \triangleq \frac{1}{\Gamma(k)} \int_x^\infty u^{k-1} e^{-u} du, \quad \Gamma(k) = \int_0^\infty u^{k-1} e^{-u} du. \quad (\text{B.7})$$

- **Special Case: Distinct Rates**

If all rates are distinct, then the sum follows a standard hypoexponential distribution with a closed-form CCDF as

$$F_\Lambda(\lambda) = \sum_{m=1}^K e^{-\mu_m(\lambda - \lambda_0)_+} \prod_{\substack{j=1 \\ j \neq m}}^K \frac{\mu_j}{\mu_j - \mu_m}. \quad (\text{B.8})$$

However, this expression becomes numerically unstable for nearly equal rates.